Impediments to Predicting Site Response: Seismic Property Estimation and Modeling Simplifications

by Eric M. Thompson, Laurie G. Baise, Robert E. Kayen, and Bojan B. Guzina

Abstract   We compare estimates of the empirical transfer function (ETF) to the plane *SH*-wave theoretical transfer function (TTF) within a laterally constant medium for invasive and noninvasive estimates of the seismic shear-wave slownesses at 13 Kiban-Kyoshin network stations throughout Japan. The difference between the ETF and either of the TTFs is substantially larger than the difference between the two TTFs computed from different estimates of the seismic properties. We show that the plane *SH*-wave TTF through a laterally homogeneous medium at vertical incidence inadequately models observed amplifications at most sites for both slowness estimates, obtained via downhole measurements and the spectral analysis of surface waves. Strategies to improve the predictions can be separated into two broad categories: improving the measurement of soil properties and improving the theory that maps the 1D soil profile onto spectral amplification. Using an example site where the 1D plane *SH*-wave formulation poorly predicts the ETF, we find a more satisfactory fit to the ETF by modeling the full wavefield and incorporating spatially correlated variability of the seismic properties. We conclude that our ability to model the observed site response transfer function is limited largely by the assumptions of the theoretical formulation rather than the uncertainty of the soil property estimates.

Introduction

The near-surface properties of the Earth (seismic slownesses, density, and attenuation) modify seismic waves as they propagate to the surface where they are recorded. This phenomenon, known as the site response, is an important factor that contributes to the seismic hazard at a given location. The site response theoretical transfer function (TTF) requires both estimates of soil properties and a theoretical model that maps the soil properties onto spectral amplifications. In this article we address the relative contribution to the uncertainty in estimating the site response transfer function stemming from (1) the experimental bias of seismic property estimates and (2) common modeling simplifications such as the assumption of plane *SH* waves propagating through a laterally homogeneous medium (we refer to the latter model as SH1D).

The attenuation of *P* and *S* waves ($Q_{p,s}^{-1}$) is typically poorly constrained but can substantially affect the observed site response. Seismic waves are attenuated by scattering ($^{Sc}Q^{-1}$) and from anelastic processes, termed intrinsic attenuation ($^{i}Q^{-1}$). Seismic scattering is the modification of seismic waves by heterogeneities within the medium. $^{i}Q^{-1}$ includes multiple physical processes, such as the conversion of seismic energy to heat through friction, viscosity, permanent deformations, and thermal relaxation. On the other hand, $^{Sc}Q^{-1}$ disperses the seismic energy within the medium

but does not remove energy from the total wavefield (Sato and Fehler, 1998).

The site response transfer function is usually represented in the frequency domain, and spectral ratios are typically used for its description (e.g., Shearer and Orcutt, 1987; Steidl, 1993; Field and Jacob, 1995; Steidl *et al.*, 1996; Bonilla *et al.*, 2002). Spectral ratios allow us to compare the frequency content of two ground-motion records. Assuming that the observed seismogram is the combination of linear time-invariant systems (source, path, site, and instrument), we can isolate the site response by dividing the spectrum of a recording that includes site response by the spectrum of a recording that contains no site effects. Thus, we must assume that the source, path, and instrument effects are identical for both recordings (Borcherdt, 1970). When attempting to isolate the site response, two types of ground-motion pairs are typically used: a soil-outcrop pair where both are recorded at the free surface but located on different geologic units or a surface-downhole pair. A soil-outcrop pair is valuable because in theory, the spectral ratios represent exactly the transfer function needed for predicting the ground motion of a soil site from a synthetic ground motion or a previously recorded ground motion. A surface-downhole pair, on the other hand, is the transfer function that most directly measures how the seismic properties of the near-surface materials modify the

incoming seismic waves. We analyze only surface-downhole recording pairs in this article.

Many studies have preferred the use of soil-outcrop pairs to estimate site response when analyzing soil behavior. For example, Darragh and Shakal (1991), Seed et al. (1991), and Youd and Carter (2005) used the ground motion at Yerba Buena Island as the bedrock reference site to estimate the site response at Treasure Island. But Baise et al. (2003) used the coherency and correlation coefficient of the downhole Treasure Island waveform with the surface and downhole waveforms at Yerba Buena Island to show that Yerba Buena Island is not an appropriate reference site for Treasure Island. Possible explanations include that (1) the Franciscan bedrock in the San Francisco Bay is highly deformed and causes the seismic response to vary over short distances, and (2) wave propagation in the San Francisco Bay sediments is a combination of vertically-propagating S-waves and horizontally-propagating surface waves, the latter of which cannot be included in one-dimensional (1D) models. Further, Abercrombie (1997) showed that even crystalline rock exhibits significant site response because the seismic quality factor (Q) decreases considerably near the surface, regardless of rock type, and that these low values of the quality factor can extend to 1.5 km depth. The difficulty in finding an appropriate outcrop reference site for a soil recording is one reason we use surface-downhole recordings in this article.

The disadvantage most frequently cited for surface-downhole pairs is that the seismic waves are recorded twice: once as they propagate towards the surface and again after being reflected at the free-surface. This causes the resulting spectral ratios to exhibit a fundamentally different response than the usual definition of site response. Thus, the empirical transfer function (ETF) from the surface-downhole pair cannot be directly applied to an outcrop because it does not exhibit this downgoing-wave effect. In general, previous recordings are taken on the surface, and numerical models predict synthetic seismograms at the surface.

The fundamental problem for both the soil-outcrop and surface-downhole pairs is that the predicted amplifications rarely match the observed amplifications in blind prediction experiments (Boore, 2004). For engineering applications where simplicity is a virtue, such predictions generally presuppose that the SH1D assumption with vertical incidence is correct. In this article we show that this is a questionable assumption that in many cases may be inappropriate.

One might reasonably expect that the discrepancies between predicted and observed site response results from the errors in the seismic property estimates. To test this hypothesis, we compare invasive and noninvasive estimates of the near-surface seismic properties at 13 Kiban-Kyoshin network (KiK-net) surface-downhole pairs in Japan. Each estimate of the seismic properties results in an independent estimate of the site response transfer function. By comparing these two independent estimates of the TTFs at each site to the ETF derived from 10 independent ground-motion pairs, we are able to separate the effects of (1) the approximations under-

lying the theoretical formulation and (2) the bias in the seismic property estimates. By including only ground motions with maximum acceleration less than 2.0 m/sec², we isolate the linear wave propagation behavior so that our results cannot be confounded with nonlinear soil behavior. We then progress from the simplest theoretical formulation (SH1D and vertical incidence) to more complete and realistic representations of the medium and wavefield to determine if we can improve the fit to the observed data by adding complexity to the theoretical model. The SH1D TTFs for the two independent profiles are similar at all 13 sites and accurately model the ETFs at a minority of the sites. Generalizing the calculation to include the full three-dimensional (3D) wavefield with spatially variable properties substantially improves the fit to the ETF at an example site that cannot be modeled by the SH1D TTF.

The Downgoing-Wave Effect

As discussed previously, there are two types of site response pairs from which we can estimate the transfer function, and we have chosen to study the ETF at surface-downhole receivers. We compare the ETF at each site to two different SH1D TTFs. Because we are unable to isolate the upgoing wave ($\acute{u}_d$) from the reflected downgoing wave ($\grave{u}_d$) we must account for the interaction of these waves, termed the downgoing-wave effect. We refer to the TTF that includes the downgoing-wave effect as

$$\text{TTF}_u = \frac{u_s}{u_d} = \frac{u_s}{\acute{u}_d + \grave{u}_d}, \tag{1}$$

where u_s and u_d are the complete surface and downhole displacement responses, and $\acute{u}_d$ and $\grave{u}_d$ are the downhole displacements of the upgoing and downgoing waves. The subscript u in equation (1) indicates that the reference condition includes the complete downhole response. Shearer and Orcutt (1987) provide a more thorough discussion of the downgoing-wave effect than we can provide in this article. Bonilla et al. (2002) refer to the TTF_u response as the borehole response. The destructive interference of the upgoing and downgoing waves creates spectral holes in the u_d response. This effect is diminished if the wave is scattered between the downhole receiver and the free surface. Thus, we also compute the surface response relative to $\acute{u}_d$ only

$$\text{TTF}_{\acute{u}} = \frac{u_s}{\acute{u}_d}, \tag{2}$$

which removes the downgoing-wave effect. Bonilla et al. (2002) refer to $\text{TTF}_{\acute{u}}$ as the outcrop response. This term is potentially misleading because the reference condition is not at the free surface. The $\text{TTF}_{\acute{u}}$ response assumes that an external mechanism removes the downgoing wave, which is not part of the theoretical formulation. Thus, if the $\text{TTF}_{\acute{u}}$ response fits the ETF, then we can conclude that the downgoing-wave effect is diminished, but the physical mechanism

responsible for this must be inferred through other methods or observations.

Data

Surface-Downhole Data: The KiK-Net Strong-Motion Network

The KiK-net strong-motion network in Japan provides numerous surface-downhole station pairs that have recorded earthquakes over a wide range of magnitudes and peak ground accelerations (see the Data and Resources section; Aoi *et al.*, 2000; Okada *et al.*, 2004). KiK-net also provides downhole logging estimates of the seismic structure for each surface-downhole station discussed in this article.

Table 1 gives the maximum depth (D_{max}), the NEHRP site class (International Code Council [ICC], 2006), the travel time averaged *S*-wave velocity of the upper 30 m [V_{S30}] of the two different velocity estimates, and the variance reduction for the SH1D TTF$_u$ model (defined at the beginning of the Results section). The depth of the downhole recordings corresponds to the borehole D_{max}. Note that all of the KiK-net downhole recordings are located about 100 m below the surface except for two stations (KGWH02 and HRSH01) that are located about 200 m below the surface.

At each station we estimate the ETF from 10 earthquakes. The ground motions meet three requirements: (1) the maximum acceleration of the ground motion is less than 2.0 m/sec^2 to guarantee that strains are in the linear range, (2) the signal-to-noise ratio of both horizontal components of the surface and downhole recordings are greater than five in the 1–20 Hz frequency range, and (3) the onset of the *S* wave is easily identified. Table 2 lists the events included in our analysis, and Table 3 gives the 10 earthquakes that correspond to each station. While we reused as many events as possible at different stations, the aforementioned requirements limited the number of stations that could use a specific event, increasing the total number of events in Table 2.

Invasive and Noninvasive Material Characterization

A wide variety of methods are commonly used for determining seismic slownesses of near-surface materials. In this article we compare site response estimates from both invasive and noninvasive methods. Downhole logging is an invasive method, which may be considered one of the most direct and precise methods for measuring seismic slownesses. Boore and Asten (2008) compared slowness estimates by various invasive and noninvasive methods in a blind comparison study. They found that linear site amplifications from the various methods are generally within 20% of each other. Moss (2008) used the coefficient of variation (c_v) as a measure of the uncertainty of V_{S30} estimates; c_v is a normalized estimate of the variability of a sample defined as the ratio of the standard deviation to the mean. Moss (2008) compiled V_{S30} estimates from various methods and found that c_v is about 0.01–0.03 for colocated invasive methods, 0.05–0.06 for colocated noninvasive methods, and 0.20–0.35 for measurements within the same geologic units as defined by Wills and Clahan (2006).

Downhole methods are generally considered the most accurate and direct measurement of the seismic slownesses in common use. Still, the slowness estimates may be biased if soil disturbance alters the seismic travel times in the vicinity of the measurement (Moss, 2008). The raw downhole travel-time measurements have been simplified to produce relatively coarse piecewise constant profiles prior to being distributed via the KiK-net Web site. Thus, we cannot test the effect of the limited resolution of these profiles in this article. But Boore and Thompson (2007) showed that approximating detailed *PS* suspension log measurements with 10 m thick constant-slowness layers has negligible effects on the predicted amplification factors below approximately 5 Hz. Thus, large residuals between observed and predicted amplifications below 5 Hz cannot be attributed to a lack of precision of the soil profile.

In this article we compare the downhole *S*-wave slowness (S_s) estimates and the resulting theoretical site response

Table 1
Station Summary

Site	SASW				Downhole			
	D_{max}, m	V_{S30}, m/sec	Site Class	VR	D_{max}, m	V_{S30}, m/sec	Site Class	VR
SMNH01	94	477	C	0.56	101	464	C	0.72
TTRH02	97	284	D	0.50	100	310	D	0.37
OKYH09	117	538	C	0.22	100	505	C	0.12
SMNH02	241	555	C	0.46	101	503	C	0.47
WKYH03	179	577	C	−2.83	100	547	C	−5.59
WKYH01	176	482	C	−0.31	101	463	C	−0.25
NARH01	149	382	C	0.60	100	338	D	0.55
OSKH03	89	406	C	−1.47	100	426	C	−0.82
KGWH02	98	217	D	0.56	200	183	D	0.64
HRSH01	158	428	C	0.39	205	403	C	0.28
OKYH07	96	912	B	−0.43	100	929	B	−0.60
HYGH10	99	201	D	0.71	100	224	D	0.74
HYGH07	123	521	C	−0.44	100	506	C	−1.87

Table 2
Earthquakes Used to Compute the Empirical Transfer Functions

ID	Date (dd/mm/yy)	Time (hr:min:sec)	M_w	Latitude	Longitude	Depth (km)
1	16/03/99	16:43:00	4.9	35.2670	135.9330	12
2	17/04/99	17:31:00	3.8	34.9670	134.7170	18
3	16/07/99	02:59:00	4.4	34.4170	133.2000	20
4	21/08/99	05:33:00	5.4	34.0500	135.4670	70
5	27/02/00	00:03:00	3.9	35.2020	135.5470	15
6	16/05/00	04:09:00	4.3	34.9630	135.5000	16
7	02/06/00	15:06:00	4.0	34.0220	135.3930	62
8	17/07/00	08:00:00	4.3	35.3720	133.4220	17
9	27/08/00	13:13:00	4.1	34.5320	135.6500	11
10	06/10/00	13:30:00	7.3	35.2750	133.3480	11
11	08/10/00	13:17:00	5.5	35.1370	133.1520	8
12	17/10/00	22:17:00	4.2	35.1880	133.4280	12
13	31/10/00	01:43:00	5.5	34.2830	136.3450	44
14	03/11/00	16:33:00	4.5	35.3570	133.2930	10
15	05/11/00	03:00:00	3.8	35.1870	133.4280	12
16	07/12/00	23:09:00	4.2	35.3670	133.2880	12
17	05/01/01	05:15:00	4.0	33.7750	132.5320	47
18	09/01/01	13:37:00	4.6	33.5850	132.3680	50
19	12/01/01	08:00:00	5.4	35.4630	134.4920	10
20	20/01/01	05:20:00	4.7	35.5020	134.4800	12
21	20/01/01	05:27:00	4.1	35.4930	134.4850	12
22	20/01/01	07:24:00	4.5	35.4930	134.4900	11
23	24/01/01	00:03:00	4.2	35.4620	134.4850	9
24	25/01/01	19:45:00	4.4	33.9620	134.5420	53
25	08/02/01	14:12:00	4.2	33.9030	134.5000	14
26	11/02/01	09:17:00	4.3	35.4180	133.2970	13
27	24/03/01	15:28:00	6.4	34.1200	132.7080	51
28	03/04/01	21:14:00	4.4	33.7800	132.0280	67
29	25/08/01	22:21:00	5.1	35.1470	135.6600	10
30	26/08/01	14:23:00	3.9	35.3670	133.2620	12
31	13/09/01	05:43:00	4.4	33.8430	136.2170	45
32	17/09/01	17:57:00	3.9	35.0320	132.8930	14
33	02/10/01	21:14:00	4.6	33.4200	135.3350	25
34	08/10/01	11:23:00	4.1	35.2980	133.3230	8
35	15/10/01	01:53:00	4.3	33.8270	135.4230	23
36	04/01/02	16:34:00	4.0	33.9530	135.6400	12
37	24/01/02	16:08:00	4.5	35.3600	133.3230	9
38	04/02/02	06:02:00	4.4	33.5980	135.2470	38
39	06/03/02	07:12:00	4.5	35.2800	133.3330	15
40	27/05/02	17:31:00	3.9	35.1220	133.1430	9
41	04/07/02	12:38:00	3.8	34.1400	133.4280	19
42	02/09/02	18:17:00	4.0	34.0400	135.2720	8
43	16/09/02	10:10:00	5.3	35.3670	133.7420	10
44	13/10/02	19:06:00	4.7	33.3450	132.3580	43
45	06/02/03	02:37:00	4.5	35.0800	135.5670	15
46	02/04/03	01:38:00	4.2	35.1170	132.7220	11
47	27/07/03	01:55:00	3.5	34.5800	135.7180	15
48	14/08/03	23:46:00	4.6	33.5600	133.9820	37
49	31/08/03	10:41:00	4.2	33.5320	134.2700	37
50	13/12/03	12:32:00	4.6	34.5550	134.3000	15
51	13/12/03	22:07:00	3.8	35.2230	133.3070	11
52	08/06/04	08:05:00	4.5	34.2100	135.0770	8
53	08/06/04	09:04:00	4.3	34.2050	135.0720	8
54	12/07/04	21:45:00	3.9	34.9700	134.6750	11
55	05/09/04	19:07:00	6.9	33.0280	136.8000	38
56	05/09/04	23:57:00	7.4	33.1430	137.1420	44
57	07/09/04	08:29:00	6.4	33.3550	137.2950	41
58	13/09/04	01:24:00	3.5	35.0870	134.9150	10
59	21/09/04	10:13:00	4.2	34.2500	132.7580	48
60	27/10/04	21:27:00	4.4	33.6370	135.2700	39

(*continued*)

Table 2 (*Continued*)

ID	Date (dd/mm/yy)	Time (hr:min:sec)	M_w	Latitude	Longitude	Depth (km)
61	01/12/04	23:30:00	4.0	35.0350	135.8130	13
62	04/02/05	01:08:00	4.0	33.9700	135.5130	57
63	27/05/05	03:17:00	4.7	33.9990	133.7000	42
64	12/09/05	18:35:00	4.2	33.3400	135.7450	25
65	01/11/05	12:47:00	4.3	33.8200	135.0860	45
66	23/11/05	22:24:00	4.0	33.8520	135.1300	28
67	02/03/06	23:28:00	4.1	34.2090	135.2110	4
68	15/05/06	01:42:00	4.5	34.2200	135.2230	3
69	26/09/06	07:03:00	5.3	33.5020	131.8850	70
70	04/04/07	06:47:00	3.5	35.2890	133.3410	11
71	15/04/07	12:19:00	5.4	34.7870	136.4100	16
72	26/04/07	09:03:00	5.3	33.8850	133.5860	39
73	26/04/07	11:55:00	4.0	34.1140	135.3230	7
74	13/05/07	08:14:00	4.6	35.0050	132.7950	9
75	16/07/07	17:24:00	4.7	34.2570	135.9500	49
76	26/08/07	01:42:00	3.5	33.9690	135.3360	10
77	06/11/07	10:02:00	4.1	34.4720	135.6760	12
78	08/03/08	03:52:00	4.1	33.9700	132.6880	45
79	02/05/08	12:23:00	4.1	35.2000	132.7000	10
80	01/06/08	03:17:00	3.7	34.8570	134.9730	14

transfer functions to those based on the noninvasive method termed the spectral analysis of surface waves (SASW). The methods of data collection, processing, and inversion of S_s profiles employed in this article are identical to the methods described by Kayen *et al.* (2005). The key aspect of the SASW procedure is that we measure the phase velocity of Rayleigh waves as a function of wavelength. An electromechanical shaker produces vertical harmonic loading at the ground surface, which produces Rayleigh waves at discrete frequencies. A dispersion curve plots the relationship between the phase velocity and wavelength, which can also be computed from a theoretical 1D S_s profile. A nonlinear geophysical inversion finds a nonunique S_s profile for which the theoretical dispersion curve best fits the empirical dispersion curve. Thus, this is a less direct measure of the seismic slownesses than the downhole logging.

A complicating factor is that the *P*-wave slowness (S_p) is particularly poorly constrained in the SASW inversion and is typically related to S_s by assuming Poisson's ratio and the depth to the water table. Brown *et al.* (2002) discuss the range of possible values of Poisson's ratio in saturated and unsaturated near-surface soils and show that the assumed value of Poisson's ratio can influence the inversion solution. In general, estimates of density are required in addition to S_s and S_p to compute site amplifications. We use the procedure recommended by Boore (2008) for relating S_s and S_p to density, which makes use of the equations presented by Gardner *et al.* (1974) and Brocher (2005). As suggested in Guzina and Madyarov (2005), a systematic resolution of this problem can be achieved by combining the SASW procedure with its horizontally polarized counterpart, the so-called spectral analysis of Love waves (SALW) methodology.

The location of the temporary SASW seismometer array relative to the permanent KiK-net strong-motion station is a central concern for site characterization. The temporary SASW seismometer transect passed within about 10 m of the station at all of the sites. The range of depths that are constrained by the SASW measurements are also important to

Table 3

Events Contributing to the Empirical Transfer Function of Each Station

Station	Earthquake IDs									
SMNH01	51	14	43	27	12	37	34	26	19	16
TTRH02	74	79	69	37	34	72	70	26	50	39
OKYH09	74	79	72	69	50	39	37	12	8	14
SMNH02	46	79	43	39	37	34	40	32	11	30
WKYH03	7	56	57	73	68	67	60	4	53	42
WKYH01	38	36	60	35	31	52	25	42	24	33
NARH01	75	62	57	27	13	66	65	4	64	76
OSKH03	75	6	77	71	13	47	55	4	45	29
KGWH02	41	78	72	27	50	48	63	59	44	49
HRSH01	63	10	72	3	59	78	17	18	43	28
OKYH07	37	10	15	40	51	14	8	43	39	26
HYGH10	61	10	50	80	6	20	19	4	9	54
HYGH07	50	58	2	6	1	5	54	23	22	21

consider. The S_s in the vicinity of depth z controls the Rayleigh wave phase velocity at wavelengths of approximately $3z$ (Brown, 1998). Thus, the wavelengths measured in the SASW survey are constrained by the distance between the receivers (d). A first order approximation of the interval of the usable wavelengths for a single receiver pair is ($d/4, 3d$), ignoring the limitations related to the signal-to-noise ratio.

At each site we measure the phase velocity with a series of receiver spacings d. The minimum d for the SASW test at the sites presented here is 2 m with two exceptions: OKYH07 and WKYH03 where the minimums are 5 and 4 m, respectively. For $d = 2$ m, the approximate wavelength range is 0.5 to 6 m, which corresponds to an approximate depth range of 0.17 to 2 m. The maximum d is much more variable and is often limited by ambient noise or the available space to place the receiver array. The maximum seismometer spacing for the SASW test at the sites presented here is 70 m or more with two exceptions: OKYH09 and OSKH03 where the maximums are 55 and 40 m, respectively.

The SASW tests were oriented such that the KiK-net strong-motion station was located near the midpoint of the temporary array for the largest spacings when possible. Further, the location of the harmonic-wave source was held constant throughout the test. Thus, the horizontal distance to the station of the smaller SASW seismometer spacings, which constrain the very near-surface S_s, could be as large as 130 m.

Methods

The methods employed in our analysis include (1) estimation of the ETF, (2) computation of the various TTFs, and (3) analysis of spatially correlated random fields. The first section provides the details of how we estimate the ETF from recorded ground motions. We describe the computation of the exact SH1D solution in the subsequent section. Then, following Frankel and Clayton (1986), we model $^{Sc}Q^{-1}$ by including spatial variations of material properties of the medium using the finite difference (FD) method. We model the heterogeneity as random fields, characterized by the spatial autocorrelation function. The final Methods section provides an overview of random fields and the methods we employ to model seismic properties as random fields. We also discuss the observed variability of the seismic properties at an example borehole site in California, which provides empirical evidence that the materials within 100 m of the free surface can be modeled as random fields.

Empirical Transfer Function (ETF)

Numerous methods have been employed for estimating the ETF from input–output ground-motion pairs. Although parametric transfer function models, such as system identification, can improve the consistency of the estimates and provide a more rigorous treatment of the uncertainty (Baise and Glaser, 2000; Glaser and Baise, 2000), in this article we estimate the ETF using the spectral ratio method because (1) it is more commonly used in the literature, (2) it requires less processing, and (3) it is a more direct frequency domain representation of the ground motions.

Field and Jacob (1995) showed that the chi-square test fails to reject the null hypothesis that the frequency (f) dependent spectral ratios $SR(f)$ are sampled from a lognormal distribution. Assuming a lognormal distribution, the mean of $\ln[SR(f)]$ is equal to the natural logarithm of the median of $SR(f) = u_s(f)/u_d(f)$

$$\mu_{\ln(SR)} = \ln[\widehat{SR}(f)], \tag{3}$$

where $\widehat{SR}(f)$ is the median of $SR(f)$. A maximum likelihood estimate for $\widehat{SR}(f)$ is

$$\widehat{SR}(f) = \exp\left(\frac{1}{n}\sum_{i=1}^{n}\ln\left[\frac{u_{s,i}(f)}{u_{d,i}(f)}\right]\right), \tag{4}$$

where n is the number of ground motions. A large-sample $100(1-\alpha)$ confidence interval for $\widehat{SR}(f)$ is

$$\exp(\ln[\widehat{SR}(f)] \pm z_{1-\alpha/2}s_{\ln}(f)), \tag{5}$$

where z is the standard normal variate, and a maximum likelihood estimate of the standard deviation is

$$s_{\ln}(f) = \sqrt{\frac{1}{n}\sum_{i=1}^{n}\left(\ln\left[\frac{u_{s,i}(f)}{u_{d,i}(f)}\right] - \widehat{SR}(f)\right)^2}. \tag{6}$$

Because we only employ $\widehat{SR}(f)$ to estimate the ETF, these two terms are interchangeable within this article. In general, however, these terms are not synonymous because other estimates of the ETF are available.

The frequency domain resolution (Δf) required to resolve the shape of the transfer function controls the length of the S-wave time window $W = (2 \times \Delta f)^{-1}$. We are interested in frequencies from 1 to 20 Hz and require $\Delta f = 0.05$ Hz in order to resolve the peaks in the transfer function at low frequencies, thus $W = 10$ sec. The window begins 0.5 sec before the S-wave arrival to allow for a 5% cosine taper, and we smooth the spectra with a 0.5 Hz triangular smoothing window.

Initially, we treated the east–west and north–south components as independent observations of the ETF, doubling the number of spectral ratio estimates. The confidence intervals calculated from these observations were excessively large, making comparisons with TTFs uninformative. Rotating to the transverse component did not improve the consistency of the ETF estimates across different events. The two-dimensional (2D) complex time series employed by Steidl (1993) and Steidl et al. (1996) significantly improved the consistency of the ETF estimates and provides a satisfactory spectral representation of the horizontal ground motion. The increased scatter when the spectra of the horizontal

components are not combined is likely due to the uncertainty of the orientation of the downhole components.

Theoretical Transfer Functions

The simplest TTF considered in this article is the SH1D TTF. We compute the SH1D TTF_u and $TTF_{\dot{u}}$ amplification factors using the program Nrattle (written by C. Mueller with modification by R. Herrmann) included in the Boore (2005) ground-motion simulation program. The Nrattle Fortran routine calculates the Thomson–Haskell plane *SH*-wave transfer function (Thomson, 1950; Haskell, 1953) for horizontally stratified constant-slowness layers at a specific incidence angle from within a uniform-slowness half-space. The input parameters of Nrattle are the S_s, density (ρ), and ${}^iQ_s^{-1}$. We set the half-space equal to the S_s and ρ of the deepest measured layer. The Nrattle solution is exactly equivalent to the solution computed by the equivalent-linear site response program SHAKE for linear modulus reduction and damping curves (Schnabel *et al.*, 1972).

The next step is to include the full wavefield. We use the program developed in Guzina (1996) that is time-harmonic, full waveform, and assumes *n* homogeneous horizontal layers overlying the homogeneous bottom half-space ($n + 1$). The code allows for an arbitrary plane-wave incident displacement field in the form

$$u_1^{inc}(\mathbf{s}) = (l_1\Delta_p)e^{-ik_{p_{n+1}}\mathbf{l}\cdot\mathbf{s}} + \frac{m_1m_3\Delta_{sv} - m_2\Delta_{sh}}{\sqrt{m_1^2 + m_2^2}}e^{-ik_{s_{n+1}}\mathbf{m}\cdot\mathbf{s}},$$

$$u_2^{inc}(\mathbf{s}) = (l_2\Delta_p)e^{-ik_{p_{n+1}}\mathbf{l}\cdot\mathbf{s}} + \frac{m_2m_3\Delta_{sv} + m_1\Delta_{sh}}{\sqrt{m_1^2 + m_2^2}}e^{-ik_{s_{n+1}}\mathbf{m}\cdot\mathbf{s}},$$

$$u_3^{inc}(\mathbf{s}) = (l_3\Delta_p)e^{-ik_{p_{n+1}}\mathbf{l}\cdot\mathbf{s}} - \sqrt{m_1^2 + m_2^2}\Delta_{sv}e^{-ik_{s_{n+1}}\mathbf{m}\cdot\mathbf{s}},$$

$$(7)$$

where $\mathbf{s} = (s_1, s_2, s_3)$ is the position vector, $i = \sqrt{-1}$, $\mathbf{l} = (l_1, l_2, l_3)$ is the direction of the incident *P* wave with amplitude Δ_p, $\mathbf{m} = (m_1, m_2, m_3)$ is the direction of the incident *S* waves with amplitudes Δ_{sh} (horizontally polarized) and Δ_{sv} (vertically polarized), and $k_{p_{n+1}}$ and $k_{s_{n+1}}$, respectively, are the *P*- and *S*-wave numbers in the bottom half-space. For such incident field, the viscoelastic site response is computed exactly, within the framework of lateral homogeneity, via the method of propagator matrices as in Guzina and Pak (2001) that includes all multiples and mode conversions (see also Luco and Apsel, 1983).

To simulate seismic wave propagation through a 3D medium where the seismic properties are represented as random fields, we use Wave Propagation Program (WPP) version 1.1. This is an elastic FD code recently developed by Lawrence Livermore National Laboratory to model seismic wave propagation in complex 3D models (Nilsson *et al.*, 2007; Data and Resources section). As noted by Frankel and Clayton (1986), an important benefit of the FD method over theoretical studies of ${}^{Sc}Q^{-1}$ is that the FD method includes all multiple scattered waves, converted waves, diffractions, and caustics. Further, theoretical studies generally rely on the Born approximation, which assumes that the scattered wave amplitude is small (Sato and Fehler, 1998). Although much can be learned from theoretical treatments of seismic scatter, we prefer the FD method in this article because it is not encumbered by such assumptions.

The authors of WPP recommend 15 grid points per wavelength, so the maximum usable frequency $f_{max} = (15S_s^{max}h)^{-1}$ where *h* is the grid spacing, and S_s^{max} is the maximum S_s in the FD mesh. The cubic computational domain exhibits one stress free surface, and all other sides have absorbing boundary conditions (Clayton and Engquist, 1977) to prevent spurious reflections.

To approximate a vertically incident plane wave we place a point source on each node at a constant depth for the full horizontal extent of the mesh. On our computing cluster (16 2.8 GHz Intel Xeon CPUs each with 2 gigabytes of memory) the mesh is limited to 247^3 grid points. Thus, the simulation is constrained by the number of grid points in each direction (*nx*, *ny*, and *nz*) such that $nx \times ny \times nz \leq 247^3$. Letting $h = 2$ m and $nz = 128$ gives the mesh a height of 254 m and accommodates a horizontal plane of point sources at 200 m depth. The wave fronts are necessarily curved near the horizontal edges of the mesh, so we maximize the horizontal dimensions of the grid to minimize this effect in the center of the mesh where the synthetic seismograms are located. Letting $nx = ny$, the largest number of grid points in the mesh is $nx = ny \leq \sqrt{247^3/128} \approx 343.1$. Rounding to the nearest 10 m, the length and width of the mesh are both 680 m ($nx = ny = 341$).

We use a Ricker wavelet as the source time function

$$A(t, t_0, \omega) = [2\pi^2\omega^2(t - t_0)^2 - 1]\exp[-\pi^2\omega^2(t - t_0)^2],$$

$$(8)$$

where A is the amplitude of the source time function, $\omega = 10$ Hz is the frequency parameter, and $t_0 = 0.15$ sec. Figure 1 displays the source time function and the source amplitude spectrum. WPP models ${}^iQ_{p,s}^{-1}$ using the discrete relaxation functions presented by Liu and Archuleta (2006), and we model ${}^{Sc}Q_{p,s}^{-1}$ by representing the seismic S_s as spatially correlated random fields rather than homogeneous layers.

Spatially Correlated Random Fields

Spatial variations of a medium's properties scatter seismic waves, creating scattering attenuation ${}^{Sc}Q^{-1}$. We include ${}^{Sc}Q^{-1}$ by modeling the material properties of the medium as spatially correlated random fields. Seismic properties, such as $S_{s,p}$ and ρ, are typically modeled as deterministic functions. This function is often a piecewise constant or piecewise linear function of depth. This is generally acceptable if the length scale of the variability of the true seismic properties about the piecewise constant/linear function is much
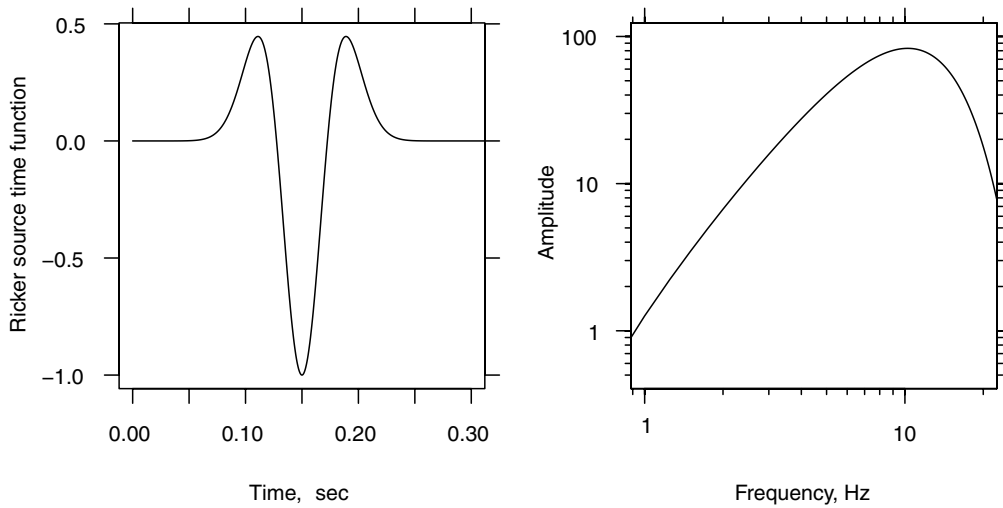
Figure 1. Temporal record (left) and Fourier amplitude spectrum (right) of the Ricker wavelet in equation (8) used in the FD simulations.

smaller than the wavelengths being modeled. For site response analysis, where we are often concerned with the behavior of waves at frequencies above 1 Hz, the assumption that these fluctuations do not influence the wavefield may not hold. In this article we model the spatial variability of the material properties as spatially correlated random fields. Following the notation of Cressie (1993) we model S_s as a random field

$$S_s(\mathbf{s}) \equiv \mu(\mathbf{s}) + \delta(\mathbf{s}), \qquad (9)$$

where $\mathbf{s} = (s_1, s_2, s_3)$ is the position vector as in equation (7), the deterministic model $\mu(\mathbf{s})$ describes the spatial fluctuation of the mean, and the correlated error process $\delta(\mathbf{s})$ includes any uncorrelated white-noise measurement error and the spatially correlated zero-mean variation of $S_s(\mathbf{s})$ about $\mu(\mathbf{s})$.

The variogram characterizes the spatial correlation structure of $S_s(\mathbf{s})$. The variogram is constructed by plotting the variance as a function of separation distance

$$2\gamma(h) = \text{var}[S_s(\mathbf{s}_1) - S_s(\mathbf{s}_2)], \qquad (10)$$

where h is the Euclidean distance between two locations $\mathbf{s}_1$ and $\mathbf{s}_2$. We often describe the spatial correlation structure with the semivariogram $\gamma(h)$. We need a parametric semivariogram model $\hat{\gamma}(h)$ to generate realizations of $S_s(\mathbf{s})$ that exhibit physically plausible spatial correlation structure. The process involves (1) constructing an empirical semivariogram from S_s estimates, (2) selecting a parametric model form, and (3) optimizing the model parameters to fit the experimental observations.

The correlation model $\hat{\gamma}(h)$ and the relevant parameters are often chosen without experimental justification because there are few examples in the literature that provide direct empirical observations of $\gamma(h)$ for seismic properties. Thus, $\hat{\gamma}(h)$ is often constrained by observations of various seismic phenomena rather than direct *in situ* measurements of the medium. For example, Frankel and Clayton (1986) use tele-

seismic travel-time anomalies, the seismic coda amplitude at high frequencies, and waveform variations across receiver arrays to constrain the correlation function of the medium. We follow an analogous approach here: we hypothesize that the site response medium is better represented by spatially correlated random media, and this improvement should be observed in the fit of the shape of the TTF to the ETF for an appropriate $\hat{\gamma}(h)$. We lack sufficient *in situ* measurements to constrain the model semivariogram $\hat{\gamma}(h)$ at the KiK-net sites, but we use empirical semivariograms from other regions to guide our model choice and the range of the parameters that we consider.

Thompson *et al.* (2007) measured the horizontal spatial variability of the near-surface sediments in the San Francisco Bay area. The empirical horizontal semivariogram of the average S-wave velocity of the upper 10 m of soil exhibited an exponential covariance function with a range of about 3 km. The exponential semivariogram model is

$$\hat{\gamma}(h) = \sigma^2[1 - \exp(-h/\phi)], \qquad (11)$$

where ϕ is the scale parameter, σ^2 is the sill, and the range is 3ϕ. This is a special case of the Whittle–Matérn correlation function

$$\hat{\gamma}(h) = \sigma^2\left[1 - \frac{2^{1-\nu}}{\Gamma(\nu)}\left(\frac{h}{\phi}\right)^\nu K_\nu\left(\frac{h}{\phi}\right)\right], \qquad (12)$$

where the sill variance $\sigma^2 > 0$, range parameter $\phi > 0$, shape parameter $\nu \geq 0$, and $K_\nu(\cdot)$ is the modified Bessel function of the second kind of order ν. The exponential correlation function is a special case of equation (12) where $\nu = 1/2$. Many different names have been given to equation (12); Guttorp and Gneiting (2005) review the different names and recommend the term Whittle–Matérn correlation model. It is frequently referred to as the Matérn model (Handcock and Stein, 1993; Ribeiro and Diggle, 2001), the von Kármán model (Frankel and Clayton, 1986; Goff and Jordan, 1988;

Sato and Fehler, 1998), and the K-Bessel model (Chilès and Delfiner, 1999) as well as others. We will first consider the exponential semivariogram model in equation (11), but the Whittle–Matérn model can be employed to control the relative amount of variability at different length scales relative to ϕ.

Figure 2 shows the suspension log measurements of S_s at the Sherman Oaks Woodman (SOW) site, from the Resolution of Site Response Issues (ROSRINE; see the Data and Resources section) project where the exponential semivariogram model fits the data well. After removing a deterministic trend, here assumed to be the horizontally layered S_s model presented by Gibbs *et al.* (1996) and a cubic smoothing spline, we see that the range in the vertical direction is about 4–6 m. This indicates that the maximum variation is realized at a distance as short as 5 m in the vertical direction for the upper 100 m of material. The range of the variability is almost certainly larger in the horizontal direction because of

the depositional process of sedimentary geologic materials. Assuming an anisotropy factor of 10 to 20 indicates that a reasonable interval for the horizontal range is 50 to 100 m.

Although some of the variability in Figure 2 could be due to measurement error, the strong spatial correlation is additional evidence that the scatter is mostly real because measurement error is generally uncorrelated. Boore and Asten (2008) argue that interpreting scatter within geologic units as measurement error is contradicted by the observation of Wentworth and Tinsley (2005) that these variations are correlated to variations in grain size. The model semivariogram is positive at $h = 0$, however, indicating a nugget effect for both deterministic trend interpretations so some of the variability is not spatially correlated. Although the nugget effect is similar for the two different models, we see that the complexity of the deterministic model influences the semivariogram. The more flexible spline model attributes more of the variability to the deterministic model, which
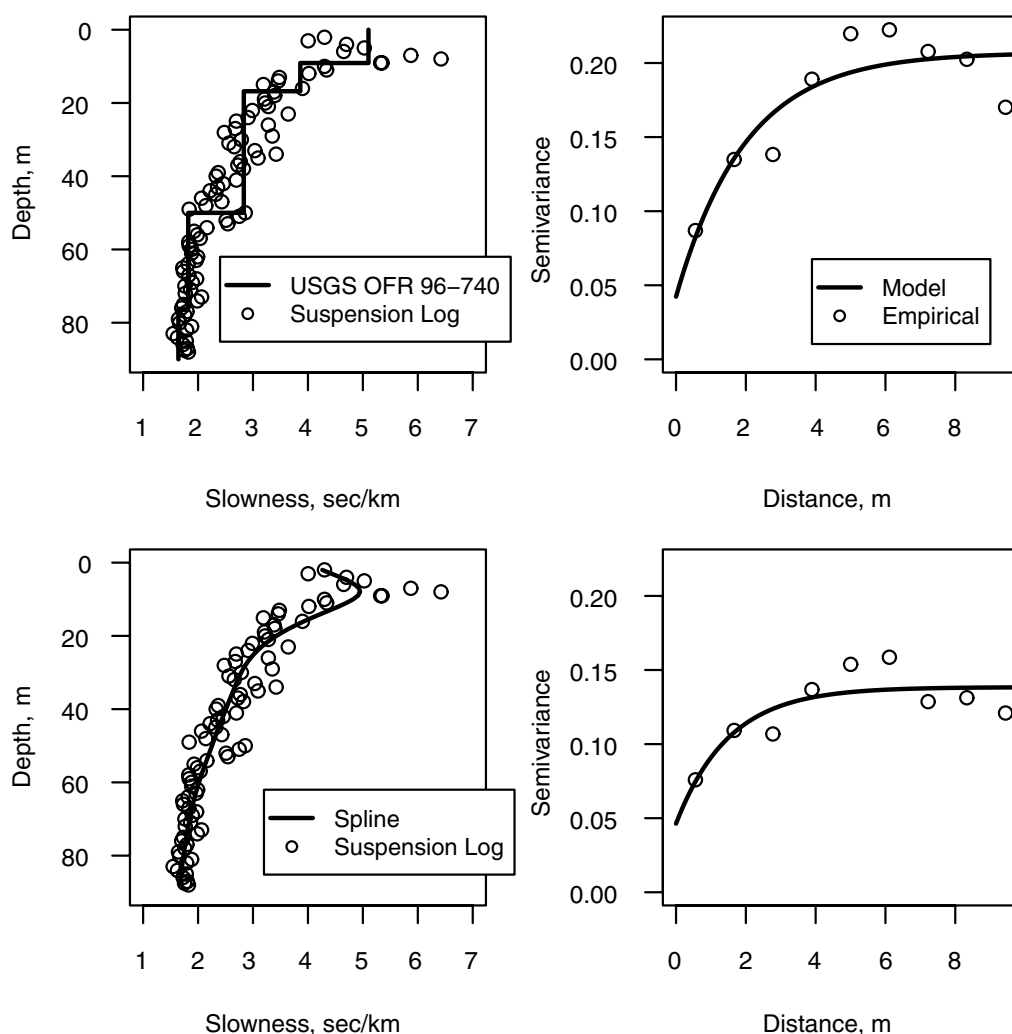
Figure 2. S_s measurements from suspension logging at ROSRINE site SOW. The vertical semivariogram of the suspension log data is computed by detrending two different deterministic models, $\mu(\mathbf{s})$. Top: Observations are detrended with the Gibbs *et al.* (1996) constant S_s model derived from surface-source downhole-receiver logging and geologic interpretations. Bottom: Observations are detrended with a spline fit to the suspension log data.

is reflected in the semivariogram by the decrease in the sill semivariance. Although the SOW site is not near the KiK-net sites, nor is it in a similar depositional environment, these empirical semivariograms are preliminary evidence that the spatial correlation structure of the upper 100 m of material could be modeled by an exponential or Whittle–Matérn model. We do not extrapolate these experimental semivariograms to the KiK-net sites.

Generating 3D realizations of random fields is computationally costly for large meshes. The program TBSIM (see the Data and Resources section; Emery and Lantuéjoul, 2006) generates 3D random fields via the turning bands method that are normally distributed with zero-mean and unit variance. We add this random field $\delta(\mathbf{s})$ to the 1D S_s profile $\mu(\mathbf{s})$ determined from downhole logging.

We must scale the variance of $\delta(\mathbf{s})$ to a reasonable value within geologic materials. Table 4 summarizes values of c_v measured for example geologic units reported by Holzer et al. (2005) and Wills and Clahan (2006). Note that these values are generally contained within the interval (0.14, 0.46) and that the Wills and Clahan (2006) values are calculated from the average S-wave velocity from the surface to 30 m depth, while the Holzer et al. (2005) values are determined from seismic cone penetration tests where the S-wave travel time is measured across 2 m intervals and is not averaged.

We assume that $\delta(\mathbf{s})$ exhibits a correlation function $\hat{\gamma}(h)$ with range parameter ϕ. The variance is a function of depth because it is constrained by the assumed c_v and the representative value for each layer. Although we lack experimental data to constrain the univariate distribution of $\delta(\mathbf{s})$, the long tails of the Gaussian distribution, which include the interval $(-\infty, \infty)$, are clearly unrealistic for geologic materials; $S_{s,p}$ and ρ are necessarily positive. It is also only possible to guarantee that the 15 grid points per wavelength requirement in the FD simulations is satisfied if the domain of S_s is bounded. Thus, we transform $\delta(\mathbf{s})$ to the beta distribution such that the set of possible values are contained within the interval (a, b). We choose the beta distribution because it is a flexible distribution, and we can define the domain and constrain the variance to solve for the distribu-

tional parameters. Johnson et al. (1994) give the probability density function for the beta distribution

$$p_{\text{beta}}(z) = \begin{cases} \frac{1}{B(p,q)} \frac{(z-a)^{p-1}(b-z)^{q-1}}{(b-a)^{p+q-1}} & a \leq z \leq b \\ 0 & \text{otherwise} \end{cases} \quad (13)$$

for $p > 0$, $q > 0$, where

$$B(p, q) = \int_0^1 x^{p-1}(1-x)^{q-1} dx = \frac{\Gamma(p)\Gamma(q)}{\Gamma(p+q)} \quad (14)$$

is the beta function, and $\Gamma(\cdot)$ is the gamma function. The expectation and variance of the beta distribution are

$$\mu_{\text{beta}} = a + \frac{(b-a)p}{p+q}, \quad (15)$$

$$\sigma_{\text{beta}}^2 = \frac{pq(b-a)^2}{(p+q)^2(p+q+1)}. \quad (16)$$

Letting $p = q$ makes the distribution symmetric about μ_{beta}. Note that $a = 0$ and $b = 1$ in the standard form of the beta distribution. The assumption of symmetry with the assumption that $a = -b$ implies that $\mu_{\text{beta}} = 0$. Figure 3 compares the density function of the standard normal with the beta distribution for the previously mentioned assumptions with various values of b, assuming unit variance. As the domain increases, the shape of the density function approaches the standard normal. The beta distribution employed in our simulations assumes $b = 2$ and $\sigma_{\text{beta}}^2 = 1$ to ensure that all realizations of $S_s(\mathbf{s})$ are within two standard deviations of $\mu(\mathbf{s})$, which implies that $p = q = 1.5$. Figure 3 shows that these values give a reasonable density function, but a value of $b \leq 1.7$ is unreasonable. To transform realizations of $\delta(\mathbf{s})$ from the standard normal to the beta distribution we first calculate the rank (r) of the n simulated values. An unbiased estimate

Table 4
S-Wave Velocity c_v by Geologic Unit

| Geologic Unit	c_v	Source
Intertidal mud (Qi)	0.244	Wills and Clahan (2006)
Quaternary-Holocene alluvium (Qal), deep	0.264	Wills and Clahan (2006)
Qal, deep, Imperial Valley	0.148	Wills and Clahan (2006)
Quaternary-Pleistocene sand deposits (Qs)	0.152	Wills and Clahan (2006)
Tertiary sandstone (Tss)	0.417	Wills and Clahan (2006)
Franciscan formation (KJf)	0.459	Wills and Clahan (2006)
Younger Bay mud	0.174	Holzer et al. (2005)
Pleistocene alluvial fan	0.138	Holzer et al. (2005)
Merrit sand	0.157	Holzer et al. (2005)
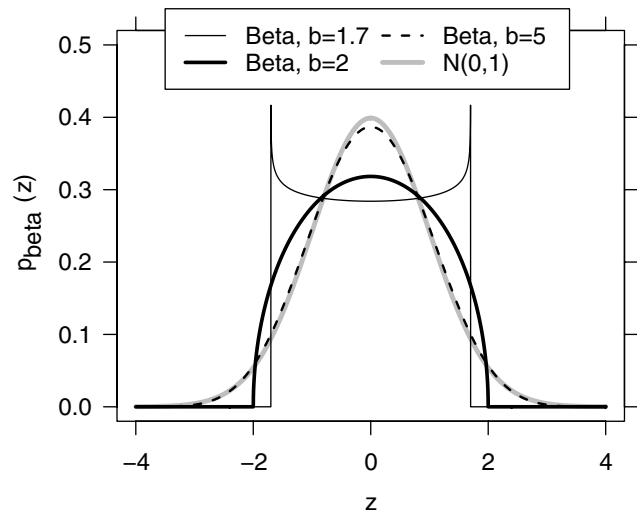
Figure 3. The standard normal distribution $N(0, 1)$ and beta density functions (equation 13) assuming $a = -b$, $p = q$, and $\sigma_{\text{beta}}^2 = 1$ for $b = 1.7$, 2, and 5.

of the exceedance probability is $P(Z > z) = r(n + 1)^{-1}$ and the inverse beta distribution function $F_{\text{beta}}^{-1}[P(Z > z)]$ gives the transformed values.

Results

Strategies for improving site response transfer function predictions can be separated into two broad categories: (1) improving the soil property measurements or (2) improving the theory that maps the 1D soil profiles to the theoretical transfer function. If the S_s profiles are inaccurate, improving the theoretical model is futile. In this section we first examine the reliability of 1D S_s profiles. Our subsequent analyses assume the soil properties estimates are sufficiently accurate to predict the ground-motion response, starting with the simplest theoretical model where we can only vary $^iQ^{-1}$ and incidence angle for the SH1D assumptions. We then progress to more complete and realistic models of the medium and the wavefield. Next, we vary $^iQ^{-1}$ and incidence angle for the full 1D wavefield, but the medium is still limited to 1D homogeneous layers. In the final Results section we analyze the full wavefield in which the medium may contain arbitrarily complex 3D heterogeneity. In this section we use the variance reduction (VR) as a goodness-of-fit parameter

$$\text{VR} = 1 - \frac{\sum_{i=1}^{n}[\text{TTF}(f_i) - \widehat{\text{SR}}(f_i)]}{\sum_{i=1}^{n}[\widehat{\text{SR}}(f_i)]^2}, \qquad (17)$$

where n is the number of frequencies at which $\widehat{\text{SR}}(f)$ is computed. The range of VR is $(-\infty, 1)$. If $\text{VR} = 1$, then the predictions exactly match the observations, and smaller values indicate poorer fit. To ensure that the values of VR are consistent across the different methods, we only include amplification predictions between 1 to 14 Hz in all cases because $f_{\max} \approx 14.2$ Hz for the FD simulations.

Reliability of 1D Slowness Profiles

The two independent estimates of the S_s profiles in Figure 4 show that subjectively the profiles are similar. Substantial differences occur in some profiles, especially within 10 m of the surface (e.g., TTRH02 and OKYH07). A goodness-of-fit measure is not appropriate here because we are only concerned with the differences in the TTFs produced by the different estimates of the material properties.

Figure 5 compares the ETF with the TTF_u response for vertical incidence and $^iQ_s = 12.5$, while the $\text{TTF}_{\ddot{u}}$ response is shown in Figure 6. We see that the TTF_u is substantially different than the ETF in many cases. The larger discrepancies in Figure 5 are comparable to those observed at KiK-net site IWTH04 by Assimaki and Steidl (2007). Note that the TTFs derived from the downhole logging and SASW profiles are similar at all the sites. Figure 6 shows that the $\text{TTF}_{\ddot{u}}$ responses are more representative of the ETF at many sites because the TTF_u responses tend to predict extreme peaks
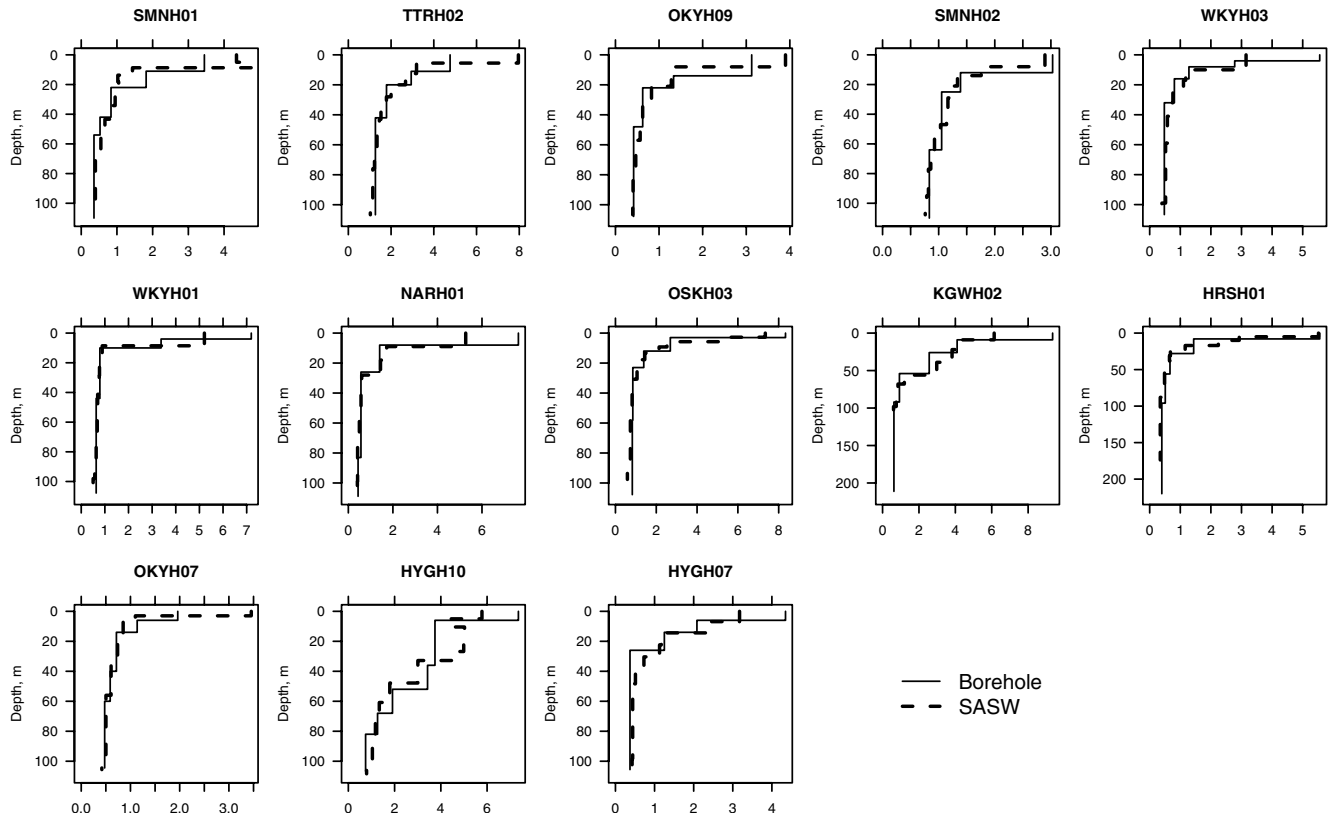

Figure 4. S_s profiles estimated by downhole logging and SASW method at each site. The units of the horizontal axis are S_s, sec/km.
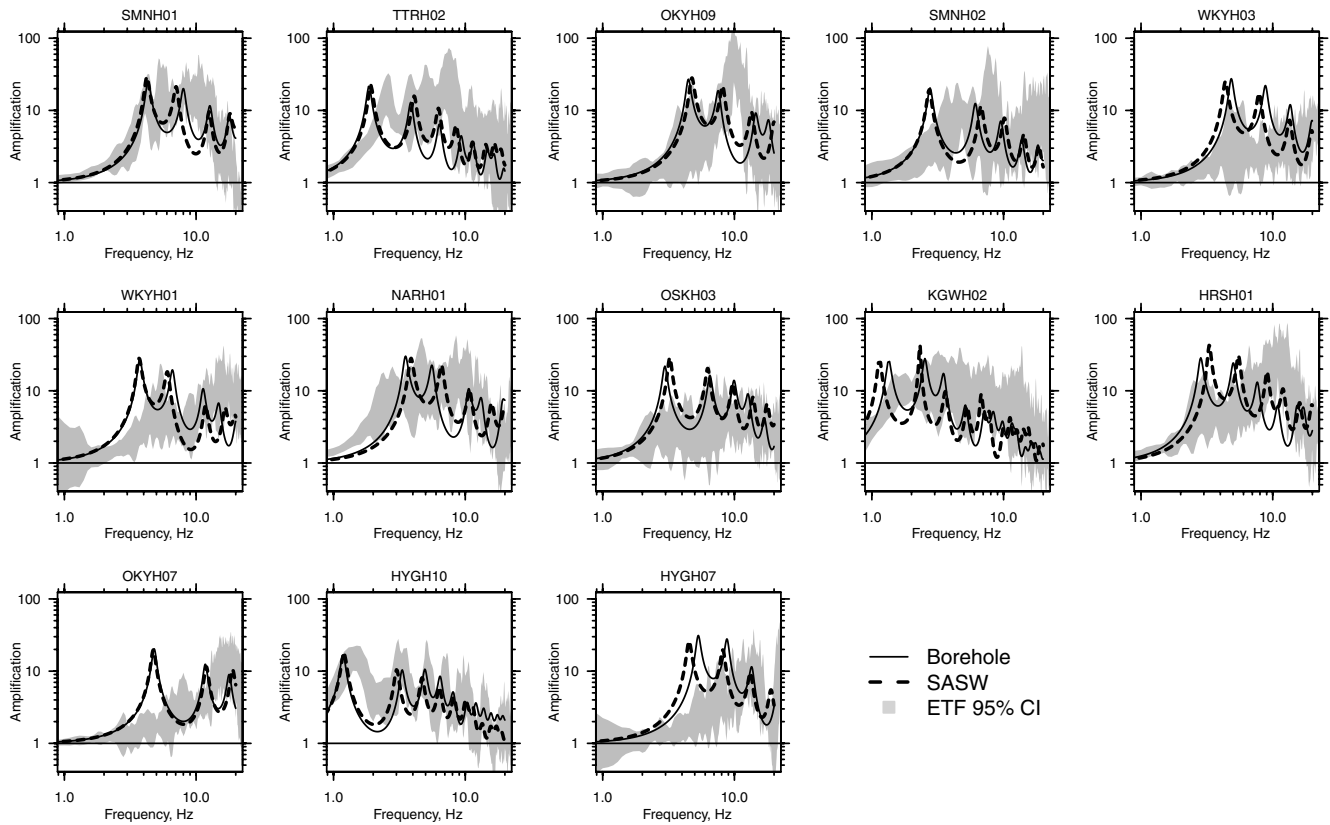
Figure 5.   The ETF 95% confidence interval (equation 5) versus TTF_{u}, computed by Nrattle using the SASW and downhole profiles with $^{i}Q_{s} = 12.5$.

and troughs that are not present in the ETF. The $TTF_{ú}$ responses, however, approach an amplification of two at low frequencies because of the free-surface effect, while the TTF_{u} responses and the ETFs approach unity. Thus, the $TTF_{ú}$ responses tend to predict larger amplifications than the ETF at low frequencies, and smaller amplifications than the ETF at higher frequencies. The $TTF_{ú}$ response fits the ETF best at stations WKYH03, WKYH01, OSKH03, OKYH07, and HYGH07.

For either the TTF_{u} or $TTF_{ú}$ responses, the difference between the amplifications predicted by the independent S_{s} estimates are small relative to (1) the difference between either TTF and the ETF and (2) the width of the ETF 95% confidence interval. Figure 7 shows this quantitatively: we computed the location and amplitude of the peaks in each of the TTF_{u} responses. Figure 7a plots the location (i.e., frequency) of the TTF_{u} peaks for the two independent estimates of the S_{s} profile against each other. Note that the scatter in Figure 7a increases with frequency, which we expect because smaller wavelengths are more sensitive to the differences between the S_{s} estimates. Figure 7b compares the amplitude of the TTF_{u} peaks. Because the ETF is not a smooth function exhibiting distinct peaks, we cannot compare the location of the ETF peaks with the TTF_{u} peaks. For each peak in the TTF_{u} response, Figure 7c compares the amplitude of the TTF_{u} response against the $\widehat{SR}(f)$ at the location of the re-

spective TTF_{u} peak. The VR for Figure 7b is 0.95 indicating that two independent estimates of the S_{s} profile predict similar peak amplitudes, while the VR for Figure 7c is 0.09 and 0.05, respectively, for the downhole and SASW estimates. Thus, neither of the S_{s} estimates predict the ETF accurately for the SH1D formulation. More importantly, this quantitatively shows that the difference between the amplifications predicted by the two independent parameter estimates is small compared to the difference between either TTF_{u} response and the ETF.

Plane *SH* Waves with 1D Medium

In subsequent sections we choose an example KiK-net station to focus on because we will be varying many parameters, and comparisons for all 13 sites would create an unreasonable number of figures. The most important property that we require of the example site is that it is representative of the largest discrepancies between the vertical SH1D TTF_{u} amplifications and the ETFs in Figure 5. We also choose a site that is well represented by the $TTF_{ú}$ response because we want to investigate why the $TTF_{ú}$ response models the ETF better than the TTF_{u} response at many stations, even though the downgoing-wave is surely included in the ETF at each station. A desirable attribute, although not required, is that the maximum S_{s} is small. This allows us to examine
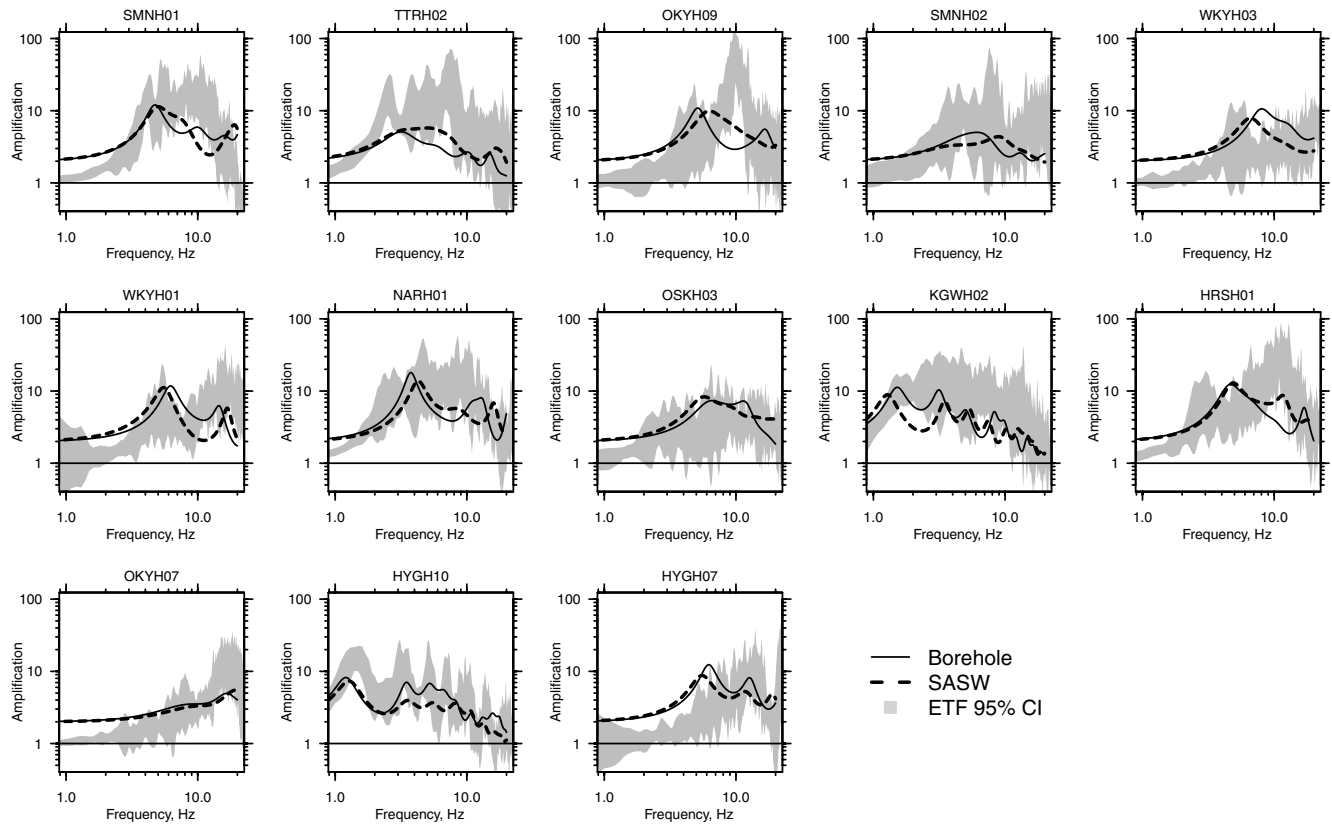
Figure 6. The ETF 95% confidence interval (equation 5) versus $TTF_{\acute{u}}$, computed by Nrattle using the SASW and downhole profiles with $^iQ_s = 12.5$.

higher frequencies for the same grid spacing in the FD calculations in the following section. Using these criteria, we select station OKYH07; the maximum S_s in the downhole profile is 1.96 sec/km, the first peaks in the TTFs are about an order of magnitude larger than the upper limit of the ETF 95% confidence interval, and the amplitude of the ETF continuously increases up to 20 Hz, which is similar to the $TTF_{\acute{u}}$ response in Figure 6. The stratigraphy at OKYH07 is 5.8 m of quaternary sand and gravel with cobbles over granite.

Within the SH1D formulation we will vary both the incidence angle and $^iQ^{-1}$. We seek empirical estimates of the incidence angles so that we can investigate if reasonably large incidences can explain the ETF. Vidale (1986) provides a method to estimate the azimuth and dip of the direction of maximum polarization from the complex data covariance matrix of a three-component seismogram. Because the S wave is polarized perpendicular to the direction of propagation, we can estimate the incidence of the direct S wave as the
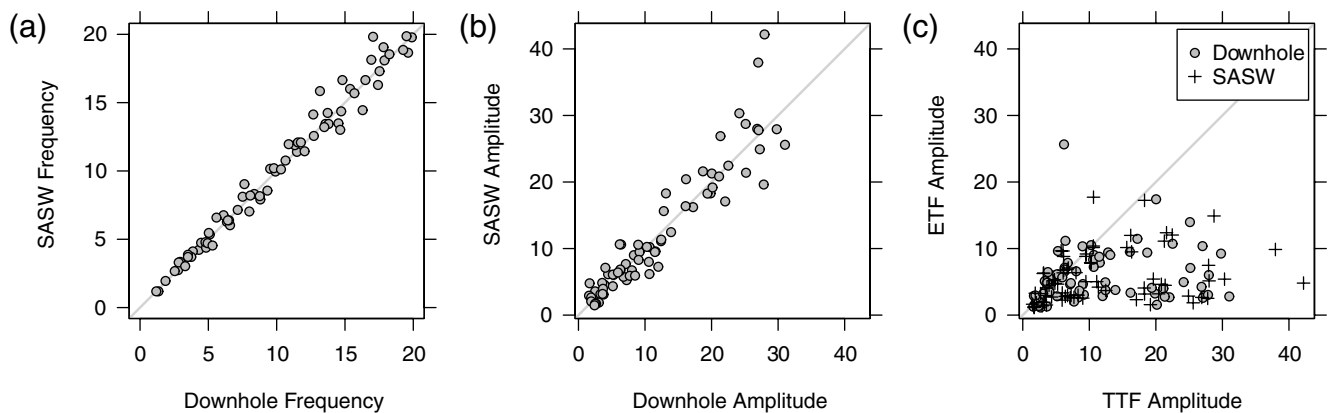
Figure 7. Comparison of (a) the frequency and (b) the amplitude of two vertical SH1D TTF_u peaks from 1–20 Hz. Comparison of (c) the TTF_u peak amplitudes with those of the ETF. The gray line in each plot is the line of equality.
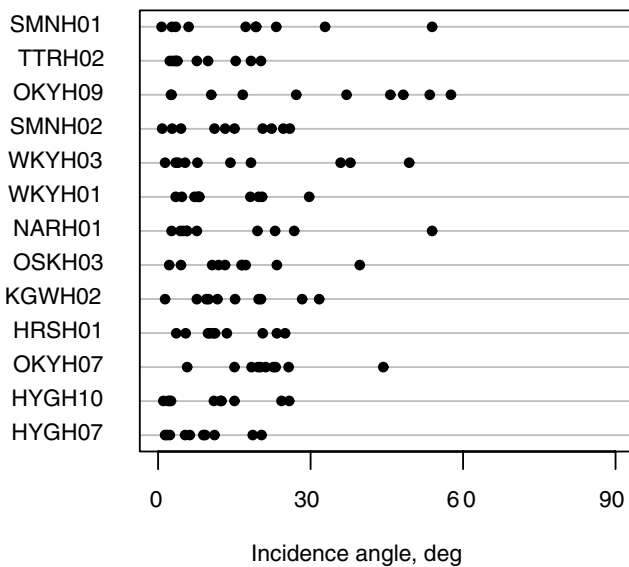
Figure 8. Estimates of the S-wave incidence angle for 10 recordings at each site using the Vidale (1986) method.

dip of the plane of maximum polarization at the onset of the S wave. The single free parameter in this analysis is the length of the time window, and we use a window 201 points wide. Figure 8 reports the incidence estimates of the direct S wave for each recording in Table 2. This shows that the incidences may be as large as 60° at some sites.

Figure 9 compares the responses to the ETF, varying ^iQ_s and the incidence angle from 0° to 60°. The incidence angle is vertical for all TTF_u responses in Figure 9a, and ^iQ_s varies from 20 to 2. The initial value of $^iQ_s = 20$ was chosen because Abercrombie (1997) reports that $^iQ_s \approx 15$ in the upper 300 m, regardless of rock type. We then decrease ^iQ_s to a minimum value of two, where we see the largest peak of the TTF is nearly within the ETF 95% confidence interval. As ^iQ_s decreases, the severity of the downgoing-wave effect is mitigated; for $^iQ_s = 20$ the VR $= -2.13$, and for $^iQ_s = 5$ the VR $= 0.57$. For $^iQ_s = 2$ the amplitude of the longest period

peak is nearly within the ETF 95% confidence interval, but the predicted amplitudes at the higher frequencies are much too small. Figure 9b illustrates the sensitivity of the TTF_u response to the incidence angle, holding $^iQ_s = 10$ constant. The choice of ^iQ_s here is arbitrary, and the influence of the incidence angle is similar for other reasonable values of ^iQ_s. As the incidence angle increases, the peaks shift to higher frequencies while the amplitudes decrease. This change is so small that the fit to the ETF is largely unaffected.

Figure 9c compares the $\text{TTF}_{\dot{u}}$ response to the ETF varying ^iQ_s. Bonilla et al. (2002) showed that the surface-downhole recordings are more similar to the $\text{TTF}_{\dot{u}}$ response than the TTF_u response for downhole receivers at depths of 220 m or more at the Garner Valley downhole array. Similarly, we see that the shape of the ETF is better modeled by the $\text{TTF}_{\dot{u}}$ response at OKYH07 because it lacks the downgoing-wave effect. Note that the depth of the downhole recording at OKYH07 is 100 m, while Bonilla et al. (2002) observed that the downgoing-wave effect was diminished at a depth of 220 m or larger. Still, the amplitude of the $\text{TTF}_{\dot{u}}$ response is consistently greater than $\widehat{\text{SR}}(f)$ at frequencies less than 10 Hz and less than $\widehat{\text{SR}}(f)$ at frequencies greater than 10 Hz. The fit improves for larger ^iQ_s; the most accurate TTF in Figure 9 is the $\text{TTF}_{\dot{u}}$ response with $^iQ_s = 100$ where VR $= 0.74$. But not only is the low-frequency response distinctively offset from the ETF because of the free-surface effect, but this is also an unrealistically large quality factor for material within 100 m of the surface.

Full Wavefield with 1D Medium

Figure 10 compares the P- and SV-wave TTF_u responses for incidence angles up to 60°. Although Figure 9b shows that the incidence angle has little effect on the SH-wave transfer function, we see that the SV phase exhibits a wide range of responses. The SV and SH responses are identical only for vertical incidence, and at nonvertical incidence the P wave contributes to the horizontal response of the recorded ground motion. The horizontal response of SV
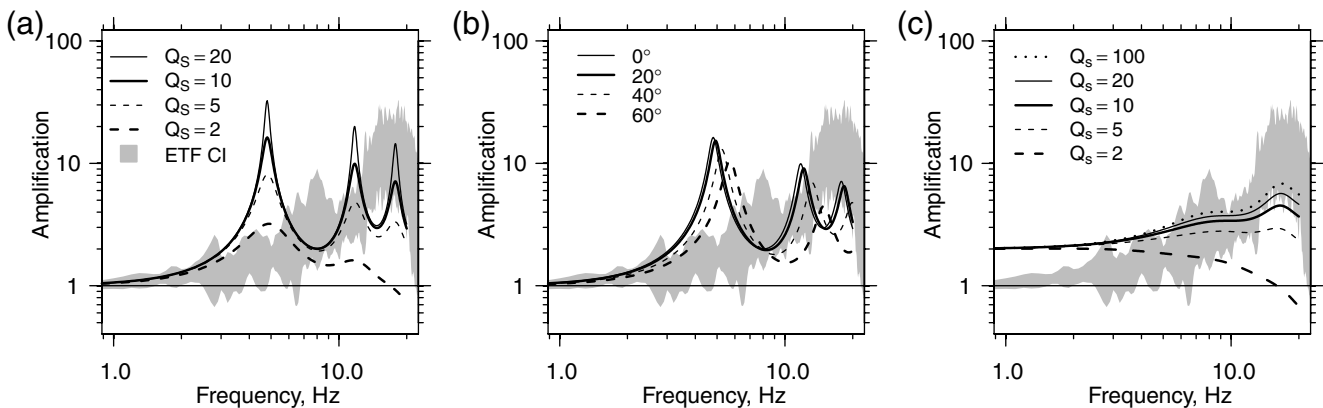

Figure 9. ETF 95% confidence interval for site OKYH07 versus SH1D TTF computed over a range of input parameters: (a) TTF_u for a range of ^iQ_s, (b) TTF_u for a range of incidence angles, and (c) $\text{TTF}_{\dot{u}}$ for a range of ^iQ_s.
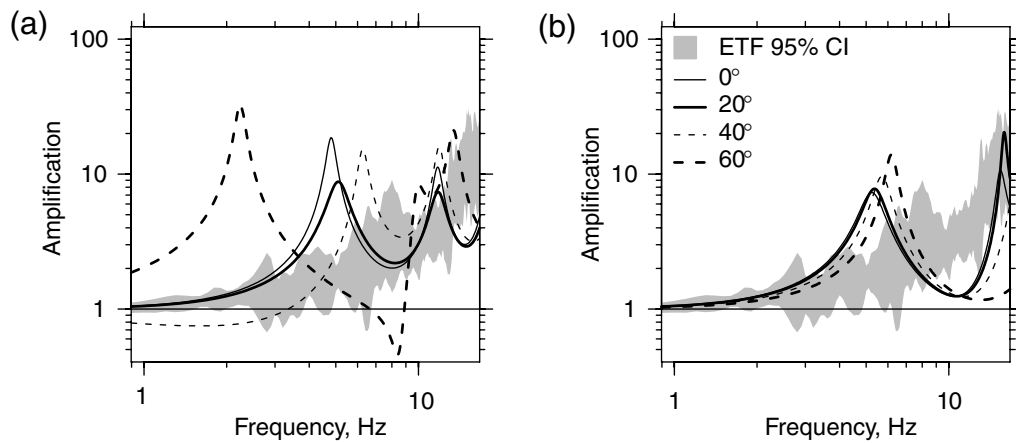
Figure 10. Variation of TTF_u for a laterally homogeneous medium for a range of incidence angles: (a) incident *SV* wave and (b) incident *P* wave.

and *SH* waves are two orthogonal components of the *S* wave polarized in the horizontal plane. The *SV* response at an angle of incidence of 20° exhibits the best fit to the ETF with VR = 0.48. This substantially improves the fit to the ETF, comparable to the improvement observed for the $\text{TTF}_{\dot{u}}$ response with ${}^iQ_s = 100$. Specifically, the amplitude of the lowest frequency peak of the *SV* response is smaller than that for the *SH* response, while the fit to the ETF at higher frequencies is not sacrificed. Further, the response approaches unity at low frequencies, matching behavior of the ETF, unlike the $\text{TTF}_{\dot{u}}$ responses that approaches an amplification of two.

Full Wavefield with 3D Heterogeneity

The solutions thus far are exact, which are only feasible because of the simplifying assumptions. By employing the FD method we sacrifice exactness in exchange for removing one assumption: the medium no longer must be laterally constant. The output of the simulations presented in this section

is three-component time series from which we estimate the transfer function using the same processing steps for estimating the ETF from ground-motion records described previously.

We must check that the FD method will produce accurate estimates of the transfer function, so first we use homogeneous layers [i.e., $\delta(\mathbf{s}) = 0$] in the FD simulation. These results should match the exact solutions in Figure 5 for vertically incident plane *S* waves. Figure 11 compares the SH1D response to the TTF_u response computed from 25 locations within the FD mesh. Note that the agreement is good, and the variability between the 25 locations is small. Sources of bias include the approximation of the plane wave with a finite number of point sources and estimating the transfer function from a time series with a finite duration (2 sec). We compute the response at these same locations in subsequent simulations, which are identical to the homogeneous case except that $\delta(\mathbf{s})$ is added to the medium. The maximum S_s in the homogeneous case is 1.96 sec/km, giving $f_{max} \approx 17$ Hz.
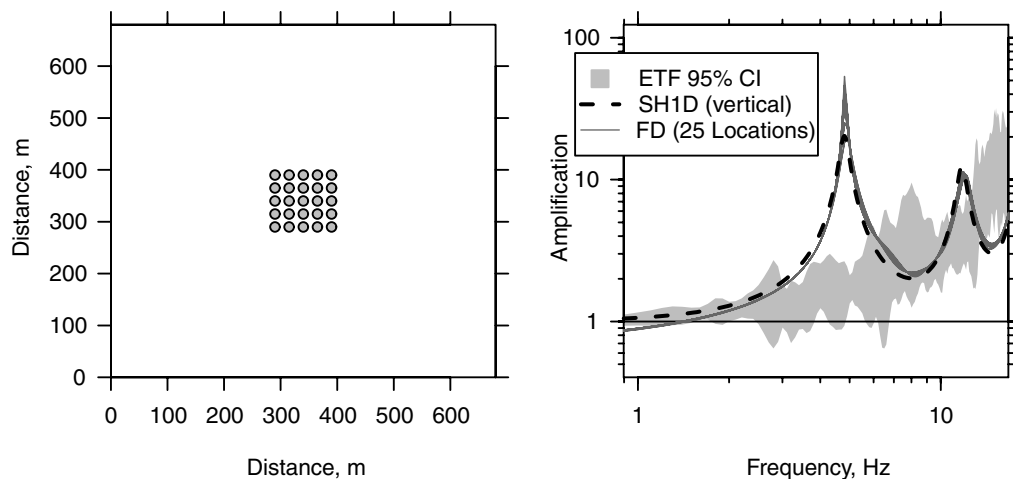

Figure 11. Verification of the FD method for calculating the TTF_u response for a laterally homogeneous medium. Left panel: Location of the 25 recordings within the extent of the FD mesh. Right panel: FD solutions versus the SH1D solution.

To limit the maximum S_s in the FD simulations, we keep $c_v = 0.1$ constant for the slowest layer while increasing c_v in the other layers. Because $c_v = 0.1$ for the first layer, even while the c_v of the other layers increases to a maximum of 0.3, the maximum possible S_s in the FD simulations is 2.35 sec /km, giving $f_{max} \approx 14.2$ Hz for all of the FD simulations presented here. We consider this range of c_v reasonable because of the empirical values reported in Table 4.

Figure 12 shows a cross section and 1D profile of the S_s model for two different realizations of the S_s random field. The distributions of both are assumed to follow the beta density function with $c_v = 0.2$ for all layers except the surface layer, and the correlation function is exponential. The scale parameter $\phi = 20$ m for the top cross section and $\phi = 100$ m for the bottom. We see that the larger ϕ produces a smoother random field $S_s(\mathbf{s})$ for the same c_v. The smoothness is a function of both ϕ and σ^2. The sill σ^2 is determined from σ^2_{beta}, which is a function of the assumed c_v. Thus, one can achieve a rougher profile by decreasing ϕ without changing f_{max} because S_s^{max} remains unchanged.

Figure 13 illustrates the influence of ϕ and σ^2. We plot the median FD TTF_u response from 25 2D complex time series of the FD simulations for a range of both parameters.

Figure 13a shows the median FD TTF_u for $\phi = 20$ to 100 m, while $c_v = 0.25$ is held constant. The median FD TTF_u for $\phi = 20$ m is most similar to the SH1D solution, but the amplitude of the transfer function above 10 Hz is slightly smaller. Similar trends occur for $\phi = 40$ and 60 m. For $\phi = 60$ m we see that the amplitude of the lowest frequency peak is slightly diminished, but when $\phi = 100$ m, the peak is almost completely removed. In Figure 13b we hold $\phi = 100$ m constant and vary c_v from 0.1 to 0.3. Note that as c_v decreases the transfer function approaches the SH1D solution.

To further investigate the details of the ground-motion response to the spatially variable S_s model we focus on the single realization of $S_s(\mathbf{s})$ that best fits the ETF from Figure 13. Figure 14 summarizes the results for the FD simulation of a realization for $\phi = 100$ m and $c_v = 0.25$. We group the 25 FD TTFs into three categories based on VR: (a) $0.77 < VR < 0.91$; (b) $0.66 < VR < 0.77$; and (c) $0.41 < VR < 0.59$. Figure 14d shows the locations of the synthetic seismograms on a map of the surficial S_s. The circles with white fill show the locations that correspond to the FD TTFs illustrated in Figure 14a, which exhibit the best fit to the ETF, while the squares with gray fill show the locations that correspond to Figure 14b with intermediate
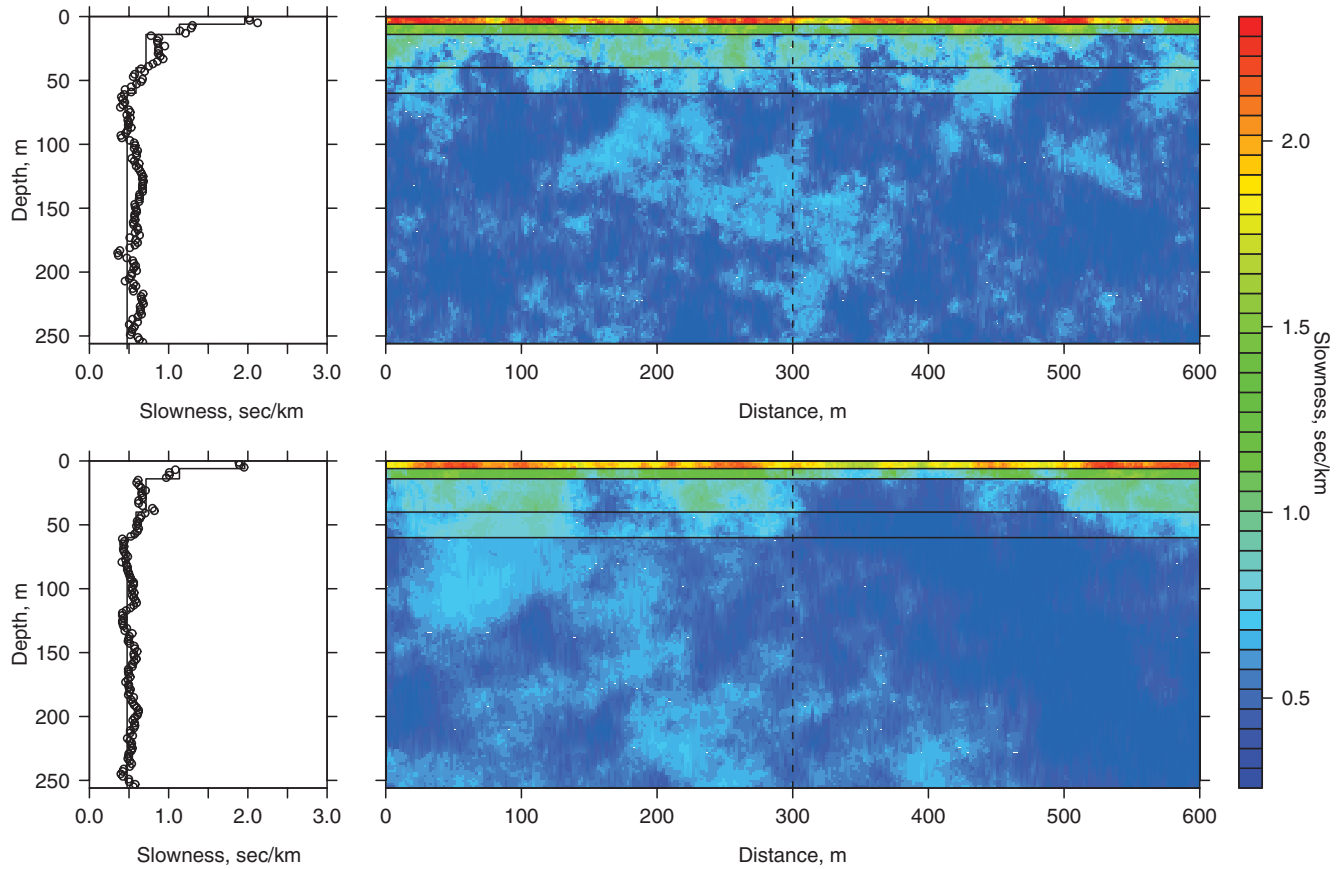

Figure 12. Summary of two random, exponentially correlated S_s distributions (top: $\phi = 20$ m; bottom: $\phi = 100$ m). Diagrams on the left are the 1D profiles along the dashed line on the 2D cross section of the 3D random field, $S_s(\mathbf{s})$. Solid lines in the 1D profiles signify the downhole layered S_s model, that is, $\mu(\mathbf{s})$.
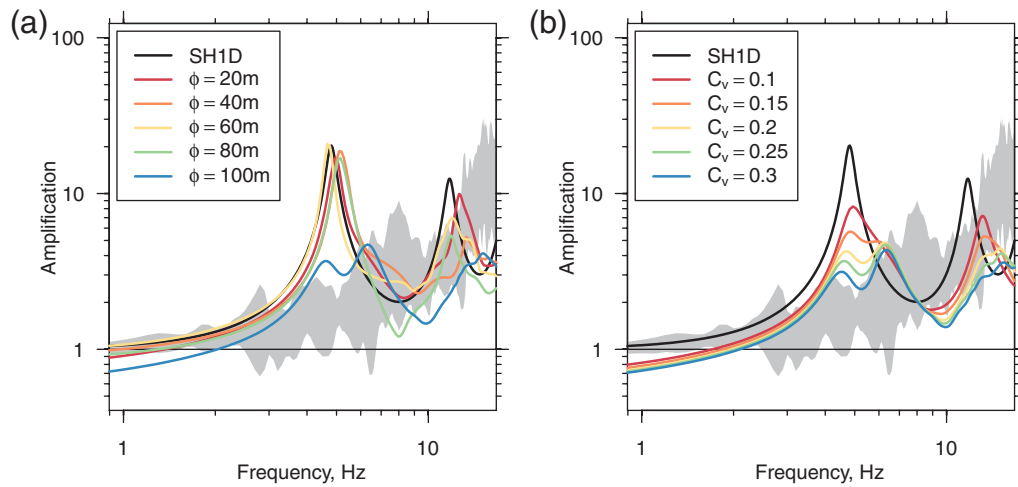
Figure 13. Estimates of $\widehat{SR}(f)$ obtained using FD simulations: (a) 20 m $\leq \phi \leq$ 100 m, $c_v = 0.25$ and (b) $0.1 \leq c_v \leq 0.3$, $\phi = 100$ m.
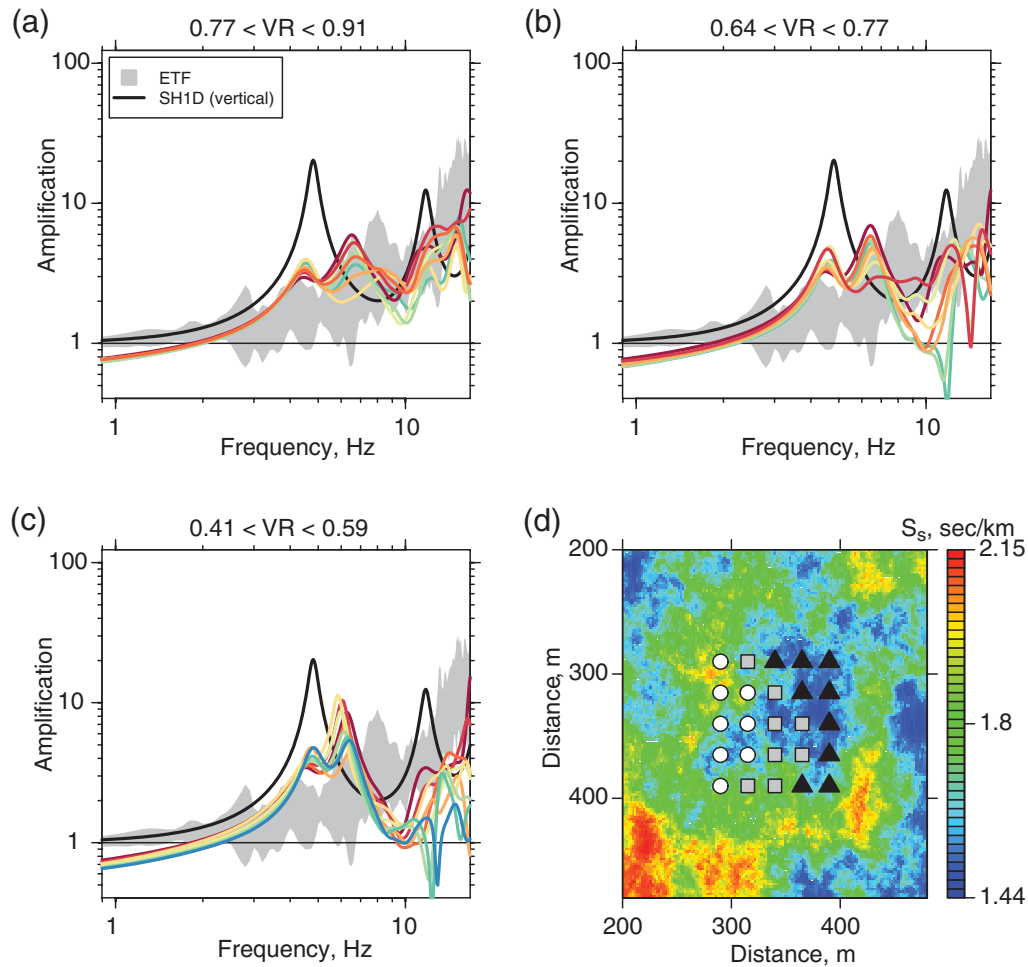

Figure 14. SH1D TTF$_u$ versus the ETF 95% confidence interval at OKYH07 and the FD TTF$_u$ responses, which includes the full wavefield and heterogeneous media ($\phi = 100$ m). Note that the FD TTF$_u$ responses are shown in color so that an individual line can be traced by eye for the extent of the plot, but the color does not indicate further information. (d) Locations of the best fitting solutions from (a) as open circles with white fill, the intermediate fit locations from (b) as squares with gray fill, and the poorest fit solutions from (c) as closed triangles.

fit, and the triangles with black fill show the locations that correspond to Figure 14c and exhibit the worst fit to the ETF. We see that the fit is quite good in some locations; the red line in Figure 14a is located almost entirely within the ETF 95% confidence interval for which VR = 0.91. At other locations the fit to the ETF is not as good, but the downgoing-wave effect is lessened at all locations.

Discussion

Nonlinearity

The initial screening of the ground motions removed all recordings with maximum acceleration of 2.0 m/sec^2 ($\approx$0.2 g) or greater. Hartzell *et al.* (2004), however, showed that the response of NEHRP class D sites can exhibit nonlinearity at frequencies greater than 2 Hz for input accelerations of 0.1 g and above. Of the 13 KiK-net sites, four are site class D when $V_S(30)$ is computed from the downhole profiles: TTRH02, NARH01, KGWH02, and HYGH10. The downhole ground motions used to estimate the ETF for these sites all have peak accelerations less than 0.1 g by chance, so nonlinearity will not affect the response at these sites for the ground motions included in our analysis.

1D Theoretical Transfer Functions

The two SH1D TTF$_u$ responses are qualitatively similar to the ETFs in Figure 5 at five sites: SMNH01, TTRH02, NARH01, KGWH02, and HYGH10. At these sites the TTFs do not fall completely within the 95% confidence interval of the ETF, but the TTF captures the general shape and amplitude of the ETF. At HYGH10 the peaks in the ETF are well resolved, and both of the TTF$_u$ responses predict the peaks relatively accurately. The similarity of the SH1D TTF$_u$ response to the ETF at these sites indicates that the true 3D variation of the seismic properties can reasonably be approximated by a laterally constant-slowness model. Also note that all of NEHRP class D sites are included in this list, indicating that slower sites are more likely to be accurately modeled by the SH1D TTF$_u$ formulation.

The TTF$_ú$ response, shown in Figure 6, better fits the ETF than the TTF$_u$ response at many sites. This indicates that the downgoing-wave effect is substantially removed at seven stations: SMNH02, WKYH03, WKYH01, OSKH03, HRSH01, OKYH07, and HYGH07. The TTF$_u$ response exhibits large peaks not present in the ETF at these sites. Bonilla *et al.* (2002) observed that the response at the Garner Valley Downhole Array exhibited similar behavior at depths of 220 m or more.

The first peak in the two TTF$_u$ responses is about an order of magnitude larger than the upper limit of the ETF 95% confidence interval at sites WKYH01 and OKYH07. The similarity of the two TTF$_u$ responses from the downhole and SASW S_s estimates indicates that the failure of the predictions to match the ETF results from limitations of the theoretical modeling rather than the uncertainty of the soil

parameter estimates. The comparisons of the TTF$_u$ and TTF$_ú$ responses to the ETF illustrate that the destructive interference of the upgoing and downgoing waves is removed, but the physical mechanism for this cannot be identified without further site-specific analysis.

The value of ^iQ_s controls the decay of the amplitude of the peaks in the TTF$_u$ response as frequency increases. But Figure 5 shows that the ETFs exhibit a distinctive increase in amplitude as the frequency increases at sites TTRH02, OKYH09, WKYH03, WKYH01, HRSH01, OKYH07, and HYGH07. This implies that no value of ^iQ_s can model the shape of these ETFs and that frequency dependent attenuation may be important. Site OKYH09 is a particularly extreme example; the ETF 95% confidence interval at 10 Hz is about (22, 125), while the downhole and SASW SH1D TTF$_u$ responses predict amplifications of 2.1 and 3.9 at 10 Hz, respectively.

The responses shown in Figure 10 for plane *SV*-waves at nonvertical incidence are substantially different than those in Figure 9 for *SH*-waves. Note that because the total response is a combination of the two orthogonal horizontal components, which includes the *P* wave for nonvertical incidence, the maximum VR = 0.48 cannot be realized for predictions unless the *S* wave contains only the *SV* component and the incidence angle is 20° for all of the *S*-wave arrivals. Figure 8 shows that the incidence angle for the direct *S* wave is highly variable across different events recorded at the same station. Thus, this specific transfer function as an explanation for the ETF is insufficient because the *SH* component is surely significant and many paths inevitably contribute to the the *S* wave, each with a unique incidence angle. Further, Dreger and Helmberger (1990) showed that the depth of the earthquake can have a significant influence on the amplitude of the direct *S* wave relative to later phases, such as multiples, which also contribute to the *S*-wave input motion. Although Figure 10 illustrates that limiting our analysis to the *SH* component of the *S* wave may substantially bias the computed site response, generalizing to the full 1D solution is still unable to model the ETF. Thus, the assumption of a laterally homogeneous medium still restricts our ability to model the observed ground motions. Removing the assumption that the medium is laterally homogeneous produces the most accurate TTFs, summarized in Figure 14.

3D Transfer Function: Rock Site

Each of the 25 FD TTF$_u$ responses for site OKYH07 in Figure 14 shows a remarkable improvement in fit to the ETF compared to the SH1D response in Figure 5. The VR for these FD TTF$_u$ responses ranges from 0.41 to 0.91, while VR = −0.60 for the the SH1D response. The improved fit to the ETF largely results from the diminished downgoing-wave effect seen in each of the individual FD TTF$_u$ responses in Figure 14.

The spatial dependence of the FD TTF$_u$ goodness-of-fit in Figure 14d is caused by the large correlation parameter of

$\phi = 100$ m. The large correlation parameter causes locations closer together to exhibit 1D profiles that are more similar than those that are further apart. The large correlation parameter also implies that the 1D profile may exhibit an offset from the *in situ* slowness estimate, in the sense that the $\delta(\mathbf{s})$ will not appear to fluctuate about the mean but could substantially bias the 1D profile to be faster or slower than $\mu(\mathbf{s})$. This leads to the question: Have we simply biased the 1D profile such that it alone can explain the ETF, and the 3D structure is not important?

We address this question with Figure 15. It compares the 1D profiles from the realization of $S_s(\mathbf{s})$ at the locations where the FD TTF_u best fit the ETF (Figure 14a; $0.77 < \text{VR} < 0.91$). We see from the profiles in Figure 15a that they are indeed generally faster than the KiK-net downhole measurements. When we use these 1D profiles from the 3D random field $S_s(\mathbf{s})$ to compute the SH1D TTF_u amplifications, we see that the peaks of the SH1D TTF_u responses in Figure 15b shift to higher frequencies. This reflects the bias in the $S_s(\mathbf{s})$ profiles shown in Figure 15a. But the deterministic trend $\mu(\mathbf{s})$ is included within the range of the profile realizations at all depths. More importantly, the maximum $\text{VR} = -0.10$ for the SH1D TTF_u responses in Figure 15b. Although this is an improvement over the original SH1D response in Figure 5, it is still much worse than any of the corresponding FD TTF_u results in Figure 14a for which $\text{VR} > 0.77$. We conclude that the diminished downgoing-wave and improved fit in Figure 14 result from the 3D seismic scattering and is not caused by the bias in the 1D profile.

Although the large range parameter may bias the 1D profiles, only realizations of $\delta(\mathbf{s})$ with a large correlation parameter can influence the transfer function at the longer wavelengths. This is important because it is at the lower frequencies where we observe the largest residuals for the SH1D TTFs. These residuals result from the interference of the upgoing and downgoing waves, which creates spectral holes in the denominator of the transfer function. Thus, the interference causes the peaks in the TTF_u response that are not present in the $\text{TTF}_{\dot{u}}$ response.

A practical concern with the FD results in Figure 14 is that we do not know which location will exhibit the best fit *a priori*. Thus, we would not be able to realize $\text{VR} = 0.91$ for predictions. The 95% confidence interval derived from the 25 FD TTF_u responses in Figure 14 is more appropriate, shown in Figure 16. We see substantial improvement in the fit to the ETF in Figure 16; the VR increases from $\text{VR} = -0.60$ for the SH1D TTF_u response to $\text{VR} = 0.73$ for the median FD TTF_u response. Further, the FD TTF_u confidence interval intersects the ETF 95% confidence interval at almost all frequencies.

3D Transfer Function: Soil Site

We have investigated site OKYH07 in great detail for two reasons: (1) it is representative of the largest discrepancies between the vertical SH1D TTF_u amplifications because the downgoing-wave effect is not observed in the ETF, and (2) it is a relatively fast site, increasing $f_{\max}$ for the FD simulations. But we are also concerned with how random media affect the site response at slower soil sites as well as sites where the downgoing-wave effect is present. Thus, we further investigate the effects of random media at site TTRH02, which is a slow soil site (NEHRP site class D). At TTRH02 the surface layer $S_s = 4.76$ sec/km ($V_S = 210$ m/sec), yielding $f_{\max} = 5.8$ Hz for the FD TTF_u results in the following section. Further, the shape of the SH1D TTF_u response in Figure 5 is similar to the ETF, but the first peak is shifted. Thus, the downgoing wave is clearly creating destructive interference at the downhole receiver. The presence of the downgoing-wave effect at TTRH02 is clear when the SH1D TTF_u response in Figure 5 is compared to the SH1D $\text{TTF}_{\dot{u}}$ response in Figure 6. Although the seismic slownesses classify TTRH02 as NEHRP site class D, the
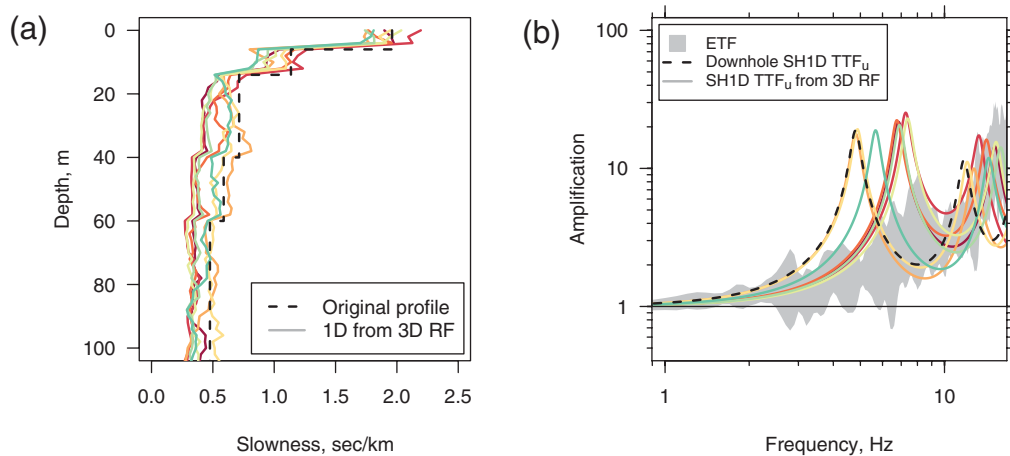

Figure 15. Diagrams of (a) the 1D S_s profiles and (b) the corresponding SH1D TTFs. The dashed line in each plot corresponds to the original downhole profile and the colors link the 1D profiles to the respective SH1D TTFs. Solid lines in each plot correspond to the 1D profile beneath the surficial location of the recordings from the 3D FD TTF_u responses that best fit the ETF (VR > 0.75) in Figure 14a.
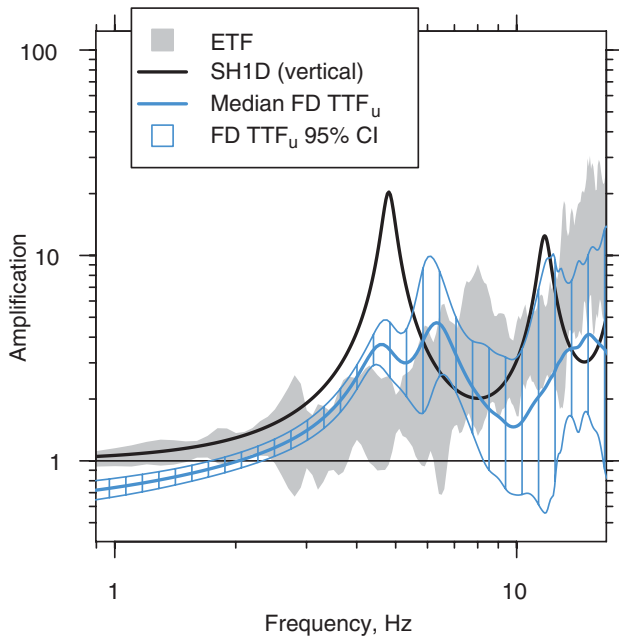
Figure 16. The 95% confidence interval for 25 FD TTF$_u$ responses in Figure 14. The VR of the median FD TTF is 0.73.

lithologic description is similar to OKYH07: 10.4 m of quaternary sand and gravel over 66.2 m of granite, followed by 6.3 m of andesite underlain by more granite.

First, we check that the FD TTF$_u$ computation compares with the exact SH1D solution for $\delta(\mathbf{s}) = 0$, shown in Figure 17a for vertical incidence and $^iQ = 12.5$. The comparison shows that these results may be less accurate than indicated in Figure 11 for site OKYH07. The FD TTF$_u$ responses are shown in Figure 17b–d for exponentially correlated random fields with $\phi = 20, 60,$ and 100 m. The $c_v = 0.25$ for all layers except the surface layer for which $c_v = 0.10$. The spatial variability for $\phi = 20$ m and 60 m does not improve the fit to the ETF. We see similar behavior for $\phi = 100$ m as we did at site OKYH07; the lowest frequency peak due to the downgoing-wave effect is removed. Here, we see that a new peak in the FD TTF$_u$ is created at about 2.2 Hz. Although the location of this peak is closer to the lowest frequency peak in the ETF, the amplitude is substantially smaller.

Site Response in Random Media

We briefly discuss the theoretical treatments of scattering and compare our results to previous research on seismic scattering to present our results in a more coherent conceptual framework.

Sato and Fehler (1998) use the travel time corrected Born approximation to estimate the frequency dependence of $^{Sc}Q^{-1}$. Although the assumptions of the Born approximation are clearly violated because the amount of variability is so large, the theoretical formulation helps interpret and un-

derstand our results. Sato and Fehler (1998) show that for random media with an exponential correlation function, the maximum $^{Sc}Q_s^{-1}$ occurs at about $(S_{s,0} \cdot \pi \cdot \phi)^{-1}$ Hz, where $S_{s,0}$ is the background S-wave slowness. Assuming $S_{s,0} \approx 0.702$ sec /km, which is the average S_s to 100 m at OKYH07, we find that the $^{Sc}Q_s^{-1}$ maximum is at about 4.5 Hz for $\phi = 100$ m. Thus, the theoretical maximum $^{Sc}Q_s^{-1}$ is very close to the lowest frequency peak in the OKYH07 SH1D TTF$_u$ response, which occurs at about 4.8 Hz. In contrast, the theoretical maximum $^{Sc}Q_s^{-1}$ for $\phi = 80$ m occurs at about 5.7 Hz. Smaller values of ϕ will shift the $^{Sc}Q_s^{-1}$ maximum to higher frequencies, away from the lowest frequency peak in the SH1D TTF$_u$ response. This explains why values of $\phi = 100$ m in Figure 13 scatter the downgoing wave at about 4.8 Hz, while the random fields with smaller values of ϕ do not. If the scale parameter ϕ decreases, then $^{Sc}Q^{-1}$ at 4.8 Hz also decreases as the maximum $^{Sc}Q^{-1}$ shifts to a higher frequency.

This article is far from the first to recognize the importance of spatially correlated heterogeneity for seismic applications. Frankel and Clayton (1986) found that a crustal model exhibiting a self-similar (i.e., von Kármán or Whittle–Matérn) correlation function with range parameter $\phi \geq 10$ km can replicate teleseismic travel-time anomalies and the seismic coda at frequencies up to 30 Hz. More recently, O'Connell (1999) showed that the magnitude dependence of site amplification observed in the 1994 Northridge earthquake, which is typically attributed to nonlinear behavior, can be explained by a model of the crust exhibiting spatially correlated variability. This is because larger earthquakes sample a larger cross section of the random media than smaller earthquakes, and the larger degree of scattering decreases the coherence of the S waves. This incoherency reduces the amplifications observed from the large earthquakes relative to smaller earthquakes. Both of these studies, however, focused on heterogeneities in the crust with fluctuations on the order of 5%–10% about the mean.

In this article we focus on wave propagation through shallow depths (100–200 m) where attenuation is greater. Correlation lengths on the order of 10 km, such as in the Frankel and Clayton (1986) and O'Connell (1999) papers, will have negligible effects on wave propagation for source-to-receiver distances of 100 to 200 m. To reproduce the ETF at OKYH07 the media must exhibit larger fluctuations (approximately 25% of the mean or greater) with a smaller range parameter ($\phi \approx 100$ m). Table 4 indicates that $c_v = 0.25$ is reasonable for V_S in many near-surface geologic materials.

The specific Whittle–Matérn (i.e., von Kármán) model considered by Frankel and Clayton (1986) assumes $\nu = 0$ in equation (12), whereas $\nu = 0.5$ in the exponential model assumed in this article. To justify our choice of ν, we must consider how it influences the frequency dependence of $^{Sc}Q_s^{-1}$. As ν decreases, the variability across shorter distances increases, all else being equal. Thus, if we employed the von Kármán model considered by Frankel and Clayton (1986), then the random fields would exhibit more variability
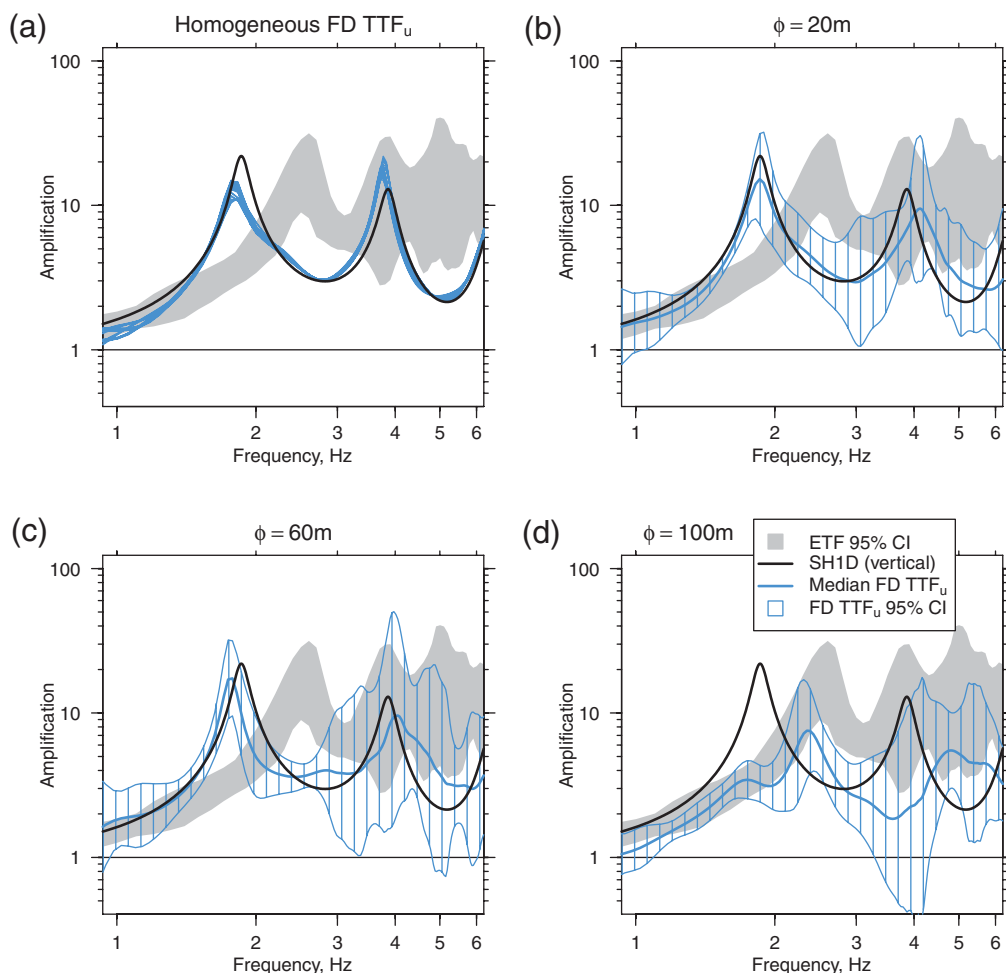
Figure 17. (a) FD TTF$_u$ for site TTRH02 computed at the 25 locations shown in Figure 11 compared with the SH1D solution. The median and 95% confidence interval for the FD TTF$_u$ derived from the 25 synthetic seismograms simulated with random media for (b) $\phi = 20$ m, (c) $\phi = 60$ m, and (d) $\phi = 100$ m.

at smaller length scales than the exponential model for the same scale parameter ϕ. Further, Frankel and Clayton (1986) note that the high frequency dependence of $^{Sc}Q_s^{-1}$ distinguishes between the von Kármán and exponential models; for the same c_v and range parameter, a von Kármán model with $\nu = 0$ would increase $^{Sc}Q_s^{-1}$ at high frequencies relative to the exponential model. But we see in Figure 5 that the ETFs generally exhibit larger amplitudes at higher frequencies than the TTFs. Thus, we expect that von Kármán model would not be preferred over the exponential model for most of the sites considered in this article.

Summary

Previous studies such as Brown *et al.* (2002), Boore and Thompson (2007), and Boore and Asten (2008) have found that the differences between invasive and noninvasive S_s profile estimates often produce only small differences in the SH1D transfer function. What distinguishes this article from previous studies is that we compare the two transfer func-

tion predictions to the ETF derived from 10 earthquakes at each site.

Including 13 sites located within a wide range of geologic conditions gives us confidence that our conclusions are reliable. Few of these sites are accurately represented by the SH1D formulation. At the sites where the ETF is not accurately modeled by the SH1D TTF, the two independent profiles predict similar amplifications. Thus, we conclude that in many cases, the assumptions of the theoretical formulation are more important than the uncertainties associated with the estimates of the material properties.

Focusing on an example rock site (OKYH07; NEHRP site class B) where the ETF is poorly modeled by the SH1D TTF, we find a satisfactory fit to the ETF only by modeling the full wavefield and incorporating spatially correlated heterogeneity of the seismic properties. The improved fit to the ETF results from seismic scattering, which removes the interference created by the downgoing-wave effect.

Further investigation of a soil site that exhibits a strong downgoing-wave effect (TTRH02; NEHRP site class D)

reveals that adding spatially correlated heterogeneity shifts the lowest frequency peak in the TTF to better match the ETF.

Data and Resources

All data analysis and plots are created using the free software R (R Development Core Team, 2008) available at http://www.r-project.org/ (last accessed July 2009) and distributed under the terms of the GNUs Not Unix General Public License version 2 or later.

The strong-motion data and downhole profiles analyzed in this article are available from the Kiban-Kyoshin Network Web site http://www.kik.bosai.go.jp/kik/ (last accessed July 2009).

The random fields were generated using the Matlab TBSIM program (Emery and Lantuéjoul, 2006). The TBSIM code is available at http://dx.doi.org/10.1016/j.cageo.2006 .03.001 (last accessed July 2009).

The 3D FD simulations are computed using the free software program WPP version 1.1 (Nilsson et al., 2007) available at https://computation.llnl.gov/casc/serpentine/ and distributed under the terms of the GNU license.

The ROSRINE data are available at http://gees.usc.edu/ ROSRINE/ (last accessed July 2009).

Acknowledgments

References

Abercrombie, R. E. (1997). Near-surface attenuation and site effects from comparison of surface and deep borehole recordings, *Bull. Seismol. Soc. Am.* **87,** 731–744.

Aoi, S., K. Obara, S. Hori, K. Kasahara, and Y. Okada (2000). New Japanese uphole–downhole strong-motion observation network: KiK-net, *Seism. Res. Lett.* **72,** 239.

Assimaki, D., and J. Steidl (2007). Inverse analysis of weak and strong motion downhole array data from the $M(\mathrm{w})7.0$ Sanriku-Minami earthquake, *Soil Dyn. Earthq. Eng.* **27,** 73–92.

Baise, L. G., and S. D. Glaser (2000). Consistency of ground-motion estimates made using system identification, *Bull. Seismol. Soc. Am.* **90,** 993–1009.

Baise, L. G., S. D. Glaser, and D. S. Dreger (2003). Site response at Treasure and Yerba Buena Islands, California, *J. Geotech. Geoenv. Eng.* **129,** 415–426.

Bonilla, L. F., J. H. Steidl, J. C. Gariel, and R. J. Archuleta (2002). Borehole response studies at the Garner Valley Downhole Array, southern California, *Bull. Seismol. Soc. Am.* **92,** 3165–3179.

Boore, D. M. (2004). Can site response be predicted? *J. Earthq. Eng.* **8,** 1–41.

Boore, D. M. (2005). SMSIM–Fortran programs for simulating ground motions from earthquakes: Version 2.3, *A revision of U.S. Geol. Surv. Open-File-Rept. 96-80-A* 55 pp.

Boore, D. M. (2008). Some thoughts on relating density to velocity, http://quake.usgs.gov/~boore/daves_notes/daves_notes_on_relating_density_to_velocity_v1.2.pdf (last accessed 24 April 2008).

Boore, D. M., and M. W. Asten (2008). Comparisons of shear-wave slowness in the Santa Clara Valley, California, from blind interpretations of data from a comprehensive set of invasive and non-invasive methods using active- and passive-sources, *Bull. Seismol. Soc. Am.* **98,** 1982–2003.

Boore, D. M., and E. M. Thompson (2007). On using surface-source downhole-receiver logging to determine seismic slownesses, *Soil Dyn. Earthq. Eng.* **27,** 971–985.

Borcherdt, R. D. (1970). Effects of local geology on ground motion near San Francisco Bay, *Bull. Seismol. Soc. Am.* **60,** 29–61.

Brocher, T. M. (2005). Empirical relations between elastic wavespeeds and density in the Earth's crust, *Bull. Seismol. Soc. Am.* **95,** 2081–2092.

Brown, L. T. (1998). Comparison of Vs profiles from SASW and borehole measurements at strong motion sites in southern California, *Master's Thesis*, University of Texas, Austin.

Brown, L. T., D. M. Boore, and K. H. Stokoe (2002). Comparison of shear-wave slowness profiles at 10 strong-motion sites from noninvasive SASW measurements and measurements made in boreholes, *Bull. Seismol. Soc. Am.* **52,** 289–300.

Chilès, J.-P., and P. Delfiner (1999). *Geostatistics: Modeling Spatial Uncertainty*, John Wiley and Sons, Inc., New York, 720 pp.

Clayton, R., and B. Engquist (1977). Absorbing boundary-conditions for acoustic and elastic wave-equations, *Bull. Seismol. Soc. Am.* **67,** 1529–1540.

Cressie, N. A. C. (1993). *Statistics for Spatial Data*, John Wiley and Sons, Inc., New York, 928 pp.

Darragh, R. B., and A. F. Shakal (1991). The site response of 2 rock and soil station pairs to strong and weak ground motion, *Bull. Seismol. Soc. Am.* **81,** 1885–1899.

Dreger, D. S., and D. V. Helmberger (1990). Broadband modeling of local earthquakes, *Bull. Seismol. Soc. Am.* **80,** 1162–1179, ISSN 0037-1106.

Emery, X., and C. Lantuéjoul (2006). TBSIM: A computer program for conditional simulation of three-dimensional Gaussian random fields via the turning bands method, *Comput. Geosci.* **32,** 1615–1628.

Field, E. H., and K. H. Jacob (1995). A comparison and test of various site-response estimation techniques, including 3 that are not reference-site dependent, *Bull. Seismol. Soc. Am.* **85,** 1127–1143.

Frankel, A., and R. W. Clayton (1986). Finite-difference simulations of seismic scattering–Implications for the propagation of short-period seismic-waves in the crust and models of crustal heterogeneity, *J. Geophys. Res.* **91,** no. B6 6465–6489.

Gardner, G. H. F., L. W. Gardner, and A. R. Gregory (1974). Formation velocity and density–Diagnostic basics for stratigraphic traps, *Geophysics* **39,** 770–780.

Gibbs, J. F., J. C. Tinsley, and W. B. Joyner (1996). Seismic velocities and geological conditions at 12 sites subjected to strong ground motion in the 1994 Northridge, California, earthquake, *U.S. Geol. Surv. Open-File-Rept. 96-740* 103 pp.

Glaser, S. D., and L. G. Baise (2000). System identification estimation of soil properties at the Lotung site, *Soil Dyn. Earthq. Eng.* **19,** 521–531.

Goff, J. A., and T. H. Jordan (1988). Stochastic modeling of seafloor morphology–Inversion of sea beam data for second-order statistics, *J. Geophys. Res.* **93,** 13,589–13,608.

Guttorp, P., and T. Gneiting (2005). On the Whittle–Matérn correlation family, Technical Report 81, University of Washington, NRCSE Technical Report Series.

Guzina, B. B. (1996). Seismic Response of Foundations and Structures in Multilayered Media, *PhD Thesis*, University of Minnesota.

Guzina, B. B., and A. I. Madyarov (2005). On the spectral analysis of Love waves, *Bull. Seismol. Soc. Am.* **95,** 1150–1169.

Guzina, B. B., and R. Y. S. Pak (2001). On the analysis of wave motions in a multi-layered solid, *Quart. J. Mech. Appl. Math.* **57,** 161–179.

Handcock, M. S., and M. L. Stein (1993). A Bayesian-analysis of kriging, *Technometrics* **35,** 403–410.

Hartzell, S., L. F. Bonilla, and R. A. Williams (2004). Prediction of nonlinear soil effects, *Bull. Seismol. Soc. Am.* **94,** 1609–1629.

Haskell, N. A. (1953). The dispersion of surface waves on multilayered media, *Bull. Seismol. Soc. Am.* **72,** 17–34.

Holzer, T. L., M. J. Bennett, T. E. Noce, and J. C. Tinsley (2005). Shear-wave velocity of surficial geologic sediments in northern California: Statistical distributions and depth dependence, *Earthq. Spectra* **21,** 161–177.

International Code Council (ICC) (2006). *International Building Code (IBC)*, Falls Church, Virginia.

Johnson, N. L., S. Kotz, and N. Balakrishnan (1994). *Continuous Univariate Distributions*, Vols. **I and II,** John Wiley and Sons, New York.

Kayen, R. E., E. M. Thompson, D. Minasian, and B. Carkin (2005). Shear-wave velocity of the ground near 60 California strong motion recording sites by the spectral analysis of surface waves (SASW) method and harmonic-wave sources, *U.S. Geol. Surv. Open-File Rept. 2005-1366* 132 pp., available from http://pubs.usgs.gov/of/2005/1366.

Liu, P. C., and R. J. Archuleta (2006). Efficient modeling of Q for 3D numerical simulation of wave propagation, *Bull. Seismol. Soc. Am.* **96,** 1352–1358.

Luco, J., and R. Apsel (1983). On the Green's functions for a layered half-space: Part I, *Bull. Seismol. Soc. Am.* **73,** 909–929.

Moss, R. E. S. (2008). Quantifying measurement uncertainty of 30-meter shear-wave velocity, *Bull. Seismol. Soc. Am.* **98,** 1399–1411.

Nilsson, S., N. A. Petersson, B. Sjogreen, and H. O. Kreiss (2007). Stable difference approximations for the elastic wave equation in second order formulation, *Siam J. Num. Anal.* **45,** 1902–1936.

O'Connell, D. R. H. (1999). Replication of apparent nonlinear seismic response with linear wave propagation models, *Science* **283,** 2045–2050.

Okada, Y., K. Kasahara, S. Hori, K. Obara, S. Sekiguchi, H. Fujiwara, and A. Yamamoto (2004). Recent progress of seismic observation networks in Japan—Hi-net, F-net, K-net and KiK-net, *Earth Planets Space* **56** XV–XXVIII.

R Development Core Team (2008). *R: A Language and Environment for Statistical Computing*, R Foundation for Statistical Computing, Vienna, Austria, http://www.R-project.org, ISBN 3-900051-07-0.

Ribeiro, P. J., and P. J. Diggle (2001). geoR: a package for geostatistical analysis, *R-NEWS* **1** 14–18, http://CRAN.R-project.org/doc/Rnews/, ISSN 1609-3631.

Sato, H., and M. C. Fehler (1998). *Seismic Wave Propagation and Scattering in the Heterogeneous Earth*, Springer-Verlag, New York.

Schnabel, P. B., J. Lysmer, and H. B. Seed (1972). SHAKE: A computer program for earthquake response analysis of horizontally layered sites, Technical Report Rept. EERC 72-12, Earthquake Engineering Research Center, University of California, Berkeley.

Seed, R., S. Dickenson, and I. Idriss (1991). Principal geotechnical aspects of the 1989 Loma Prieta earthquake, *Soils Found.* **31,** 1–26.

Shearer, P. M., and J. A. Orcutt (1987). Surface and near-surface effects on seismic-waves—theory and borehole seismometer results, *Bull. Seismol. Soc. Am.* **77,** 1168–1196.

Steidl, J. H. (1993). Variation of site response at the UCSB dense array of portable accelerometers, *Earthq. Spectra* **9,** 289–302.

Steidl, J. H., A. G. Tumarkin, and R. J. Archuleta (1996). What is a reference site? *Bull. Seismol. Soc. Am.* **86,** 1733–1748.

Thompson, E. M., L. G. Baise, and R. E. Kayen (2007). Spatial correlation of shear-wave velocity in the San Francisco Bay Area sediments, *Soil Dyn Earthq. Eng.* **27,** 144–152.

Thomson, W. T. (1950). Transmission of elastic waves through a stratified solid, *J. Appl. Phys.* **21,** 89–93.

Vidale, J. E. (1986). Complex polarization analysis of particle motion, *Bull. Seism. Soc. Am.* **76,** 1393–1405.

Wentworth, C. M., and J. C. Tinsley (2005). Geologic setting, stratigraphy, and detailed velocity structure of the Coyote Creek borehole, Santa Clara Valley, California, in *Blind Comparisons of Shear-Wave Velocities at Closely-Spaced Sites in San Jose, California*, M. W. Asten and D. M. Boore (Editors), *U.S. Geol. Surv. Open-File Rept. 2005-1169*, 26 pp., http://pubs.usgs.gov/of/2005/1169.

Wills, C. J., and K. B. Clahan (2006). Developing a map of geologically defined site-condition categories for California, *Bull. Seismol. Soc. Am.* **96,** 1483–1501.

Youd, T. L., and B. L. Carter (2005). Influence of soil softening and liquefaction on spectral acceleration, *J. Geotech. Geoenv. Eng.* **131,** 811–825.

Department of Civil and Environmental Engineering
113 Anderson Hall
Tufts University
Medford, Massachusetts 02155
eric.thompson@tufts.edu
    (E.M.T., L.G.B.)

Coastal and Marine Geology
U.S. Geological Survey
Menlo Park, California 94025
    (R.E.K.)

Department of Civil Engineering
University of Minnesota
Minneapolis, Minnesota 55455
    (B.B.G.)